

First-principles determination of spin–orbit coupling parameters in two-dimensional materials

Klaus Zollner¹, Marcin Kurpas², Martin Gmitra^{3,4} & Jaroslav Fabian¹✉

Abstract

Spin–orbit coupling (SOC) is fundamental to many phenomena in solid-state physics. Two-dimensional materials and van der Waals heterostructures provide researchers with exquisite control over this interaction; the ability to fine-tune SOC has impacts on spin transport and relaxation, topological states, optoelectronics, magnetization dynamics and even superconductivity and other correlated states. This Technical Review covers both the theoretical methodology and experimentally relevant phenomenology of SOC in 2D materials, by providing essential insights into the process of extracting the spin interactions from the underlying electronic structure obtained from first-principles density functional theory calculations. This Technical Review begins with graphene. Its SOC has a surprisingly complicated origin yet graphene remains the benchmark for other elemental centrosymmetric 2D materials in which SOC leads to a mixing of spin-up and spin-down components of the Bloch states. We then discuss spin–orbit materials, such as transition-metal dichalcogenides, in which strong SOC and the lack of space-inversion symmetry yield large spin splittings of the valence and conduction bands. This enables highly efficient optical spin orientation or robust valley Hall effect in transition-metal dichalcogenides. Next, we give guidelines for extracting the spin–orbit characteristics of van der Waals heterostructures, such as graphene/WSe₂, which serve as a platform for SOC engineering. For these representative systems, we highlight the essentials of first-principles-based methodology, including supercell formation, strain artefacts, twisting, gating and lattice relaxation. Finally, we briefly discuss the effects of proximity exchange coupling, which is another relevant spin interaction for spintronics.

Sections

Introduction

Elemental 2D solids

2D solids with broken space-inversion symmetry

Proximity effects in 2D heterostructures

Engineering spin–orbit coupling

Interplay of spin–orbit and exchange coupling

Conclusion and outlook

¹Institute for Theoretical Physics, University of Regensburg, Regensburg, Germany. ²Institute of Physics, University of Silesia in Katowice, Chorzów, Poland. ³Institute of Physics, Pavol Jozef Šafárik University in Košice, Košice, Slovakia. ⁴Institute of Experimental Physics, Slovak Academy of Sciences, Košice, Slovakia. ✉e-mail: jaroslav.fabian@ur.de

Key points

- Combining first-principles calculations with phenomenological modelling based on effective Hamiltonians enables a realistic description of the spin–orbit physics in 2D materials.
- Spin–orbit coupling (SOC) in centrosymmetric solids manifests as the lifting of degeneracies along high-symmetry lines and points in the Brillouin zone and as the spin admixture of the Bloch states. In non-centrosymmetric solids, SOC further lifts the spin degeneracy of the bands and produces spin–orbit fields (spin textures) in momentum space.
- van der Waals heterostructures enable spin–orbit and exchange coupling proximity effects through overlapping neighbouring wavefunctions (known as ‘proximitized materials’).
- Proximitized materials may exhibit qualitatively different SOC compared with pristine materials.
- Spin proximity effects in van der Waals heterostructures can be tailored by gating, straining, stacking and twisting.

Introduction

Spin–orbit coupling (SOC), a consequence of special relativity, has a profound impact on the electronic behaviour of solids^{1,2}. Initially recognized for affecting spin dynamics in electron spin resonance experiments, SOC is now the cornerstone in spin transport^{3–11}, spin–orbit torque^{12–16} and topological phenomena^{17–21}. Recently, discoveries of correlated phases that can be strongly affected by SOC have fuelled further interest^{22–25}.

How does SOC manifest in the electronic band structure? The answer is different for centrosymmetric and non-centrosymmetric materials (Fig. 1). In both classes, SOC preserves time-reversal symmetry and thus Kramers degeneracy: electrons with opposite momenta and opposite spins have the same energy. In centrosymmetric crystals, such as silicon or graphene, the energy bands are (at least) doubly degenerate. There is no spin splitting of the bands. In such crystals, SOC can be seen in the band structure as the lifting of degeneracy at certain high-symmetry lines and points of the Brillouin zone. This degeneracy lifting is a consequence of the fine structure of atomic orbitals. However, to explain, for example, the effects of SOC in spin relaxation, one needs to look at the Bloch states directly: even if two bands are degenerate, they are not eigenstates of the Pauli spin operators. SOC mixes the spin states, leading to a spin admixture commonly denoted as b^2 .

Non-centrosymmetric solids, such as GaAs or monolayer WSe₂, as well as solids in which space inversion is broken by extrinsic effects (for example, electric field) allow for a more transparent description of SOC in terms of spin–orbit fields. In such solids, the bands are no longer degenerate but spin split. This spin splitting is described by the presence of spin–orbit fields. First-principles calculations can extract these fields and enable phenomenological modelling of various phenomena based on SOC. For example, the conduction band in GaAs has spin–orbit-induced splitting, which increases with the cube power of momentum, reaching 1–10 meV for typical Fermi energies²⁶. In what ways are 2D materials unique when it comes to SOC? Most importantly, their spin properties are highly tunable by means of a number of knobs:

gating, doping, straining, twisting or stacking. It is then possible to design tunable spin functionalities based on spin transport, spin–orbit torques, topology or spin dynamics.

However, heterostructures built from 2D materials pose considerable challenges to density functional theory (DFT) simulations. For example, to construct commensurate lattice structures from disparate materials, it is often necessary to impose strain to maintain computationally manageable supercell sizes. This strain is a nuisance whose effects need to be mitigated. Another challenge is extracting the spin and orbital parameters that arise owing to proximity to neighbouring layers. Some of the questions to be addressed are: what is the range of proximity interactions? Do they affect only the neighbouring layers or do they spread further? Does it matter if the proximitizing material is a monolayer, bilayer or bulk? And ultimately, can we describe the proximity effects by simply adding new terms to the Hamiltonian describing the pristine material? That is, can we capture the relevant physics simulated on large supercells by focusing on the pristine primitive cell? This article is intended as a practical guide to provide answers to such questions.

Elemental 2D solids

We begin by describing elemental (composed of a single element) 2D solids with centrosymmetric lattices. In addition to graphene, many elemental 2D materials have been synthesized or predicted theoretically to be structurally stable^{27–31}. Most are formed by the group IV and V atoms arranged in a honeycomb lattice^{27–29,32–34}. Although the electron bands remain at least doubly degenerate, there are two principal effects of SOC: (i) opening of spin–orbit-induced gaps at K and Γ points and (ii) spin mixing of the Bloch states, characterized by spin admixture b^2 .

Group IV semimetals

Group IV materials, such as graphene or silicon, are semimetals with a direct band gap at the K -point opened by SOC (Fig. 2b). These materials crystallize in a centrosymmetric rhombohedral structure compatible with the D_{3d} point group^{35–39} (Fig. 2a). Owing to the preferred sp^3 hybridization, the lattice is buckled with out-of-plane distortion δ (graphene, whose $\delta=0$, is an exception). We collect in Fig. 2c the SOC-induced gap Δ_{so}^{Γ} and spin–orbit-induced splitting Δ_{so}^K at Γ and K . Except for graphene, the SOC-induced gaps at K are above 1 meV, making the group IV elemental semimetals suitable for exploring topological effects^{28,40–44}.

The spin–orbit gaps Δ_{so}^K at K are typically an order of magnitude less than the splittings Δ_{so}^{Γ} at Γ . The reason is that the splittings at Γ typically correspond to the fine structure of the corresponding atomic orbitals, whereas the gaps at K emerge as a result of partial sp^3 hybridization owing to the buckling of the lattice. Graphene is flat, and strictly sp^2 -hybridized, which results in the anomalously small $\Delta_{so}^K \approx 24 \mu\text{eV}$, three orders of magnitude less than the splitting at Γ . The origin of the gap Δ_{so}^K in graphene is the fine structure of d orbitals, which directly couple to p_z at K , as found by the DFT analysis⁴⁵.

Group V semiconductors

Most of the group V elemental 2D materials are semiconductors. They crystallize in the rhombohedral structure in the space group $R\bar{3}m$ (β -phase)^{46,47} and in the centrosymmetric puckered orthorhombic structure in the space group $Cmca$ (α -phase)⁴⁸ (Fig. 2b). Monolayer black phosphorus, for example, has a sizeable band gap of 2 eV, extraordinarily high carrier mobility⁴⁹ and highly anisotropic electronic properties^{50–52}. Weak SOC of phosphorus atoms is reflected in nanosecond spin lifetimes⁵³, making this material suitable for semiconductor spintronics devices.

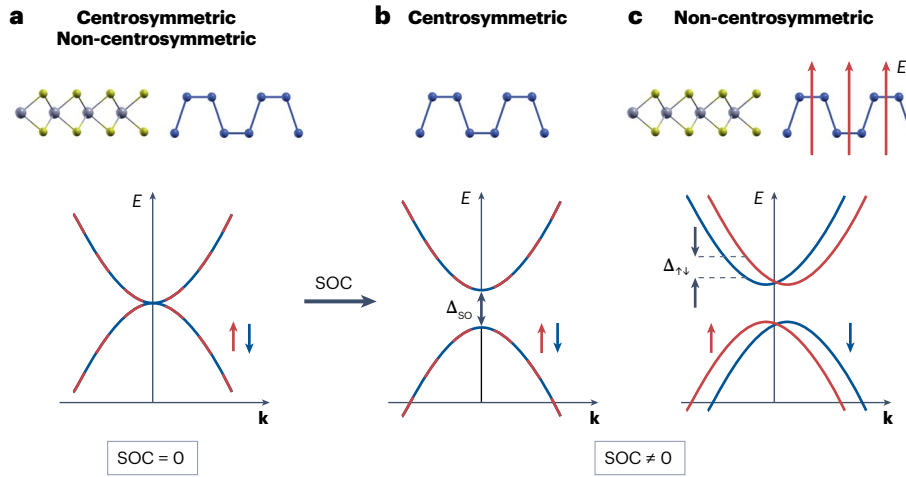


Fig. 1 | Manifestation of spin–orbit coupling in electronic band structures of crystalline solids with time-reversal symmetry. **a**, In the absence of spin–orbit coupling (SOC), the electronic states are spin degenerate in both centrosymmetric and non-centrosymmetric materials. Additional orbital degeneracy can occur at high symmetry points. For example, the Γ point ($\mathbf{k}=0$) here is fourfold degenerate. **b**, In materials with a space-inversion centre, SOC removes some orbital degeneracies, which opens spin-orbital gaps Δ_{so} , but spin states remain double degenerate at any generic \mathbf{k} -point of the Brillouin zone. **c**, For materials without an inversion centre, or when the inversion symmetry is broken, for example, by applying an external transverse electric field, the spin states split off by energy $\Delta_{\uparrow\downarrow}$, which depends on \mathbf{k} . The Kramers degeneracy $E(\mathbf{k}, \uparrow) = E(-\mathbf{k}, \downarrow)$ is preserved unless time-reversal symmetry is broken.

Z-dependence of SOC effects

In hydrogen-like ions with the atomic potential $V(r) = -Ze^2/r$, quantum mechanics predicts Z^4 dependence of the SOC strength⁵⁴. However, in atoms, the presence of core electrons screens the nuclear potential, reducing the dependence of SOC to roughly quadratic, Z^2 (ref. 55). First-principles calculations performed for selected elemental 2D materials confirm this prediction⁵⁶: $\Delta_{so}^f, \Delta_{so}^K \sim Z^2$ (Fig. 2c and Table 1).

Spin admixture b^2 . Another important ramification of SOC in centrosymmetric systems is the spin admixture b^2 . In the presence of both time-reversal and space-inversion symmetry, the Bloch states are at least twofold degenerate: at a given momentum \mathbf{k} , the band energies for spin-up and spin-down states are the same, $E(\mathbf{k}, \uparrow) = E(\mathbf{k}, \downarrow)$ ⁵⁷.

But what is the meaning of ‘spin up’ and ‘spin down’ in the presence of SOC? Clearly, the two Bloch states with opposite spin, $\psi_{n,\mathbf{k}}^\uparrow(\mathbf{r})$ and $\psi_{n,\mathbf{k}}^\downarrow(\mathbf{r})$, can, in general, no longer be the eigenstates of a Pauli spin operator. Spin is coupled to the orbital motion of the electron by means of the spin–orbit Hamiltonian $\lambda_{so}\mathbf{L} \cdot \mathbf{S}$, with \mathbf{L} being the orbital, \mathbf{S} the spin angular momentum operator and λ_{so} the SOC strength. Hence, spin is not a good quantum number and one should, in principle, refer to the quantum numbers j and j_z associated with the total angular momentum $\mathbf{J} = \mathbf{L} + \mathbf{S}$.

SOC is implemented in most major DFT codes through the generalization of the Kohn and Sham equations derived from relativistic DFT^{58,59}. Plane-wave codes^{60,61} use fully relativistic pseudopotentials^{62–64}. Codes implementing the full-potential linearized augmented plane method^{65–68} typically treat low-lying core orbitals by solving the radial four-component Dirac equation, assuming a spherically symmetric potential; SOC for the valence electrons is implemented as a second variational scheme^{69,70}.

Once SOC is included, the Kohn–Sham states $\psi_{n,\mathbf{k}}^\uparrow(\mathbf{r})$, $\psi_{n,\mathbf{k}}^\downarrow(\mathbf{r})$ become two-component spinors

$$\begin{aligned}\psi_{n,\mathbf{k}}^\uparrow(\mathbf{r}) &= [a_{n,\mathbf{k}}(\mathbf{r})|\uparrow\rangle + b_{n,\mathbf{k}}(\mathbf{r})|\downarrow\rangle]e^{i\mathbf{k}\cdot\mathbf{r}}, \\ \psi_{n,\mathbf{k}}^\downarrow(\mathbf{r}) &= [a_{n,-\mathbf{k}}^*(\mathbf{r})|\downarrow\rangle - b_{n,-\mathbf{k}}^*(\mathbf{r})|\uparrow\rangle]e^{i\mathbf{k}\cdot\mathbf{r}},\end{aligned}\quad (1)$$

in which n labels the band, whereas complex amplitudes $a_{n,\mathbf{k}}(\mathbf{r})$ and $b_{n,\mathbf{k}}(\mathbf{r})$ are lattice periodic functions. From equation (1), it is clear that $\psi_{n,\mathbf{k}}^\uparrow(\mathbf{r})$ and $\psi_{n,\mathbf{k}}^\downarrow(\mathbf{r})$ are now mixtures of pure (Pauli) spin states $|\uparrow\rangle$ and $|\downarrow\rangle$. The meaning of the superscript labels \uparrow and \downarrow , which denote

the two orthogonal degenerate states, becomes clear if SOC is a weak perturbation. Then, by convention, $a \sim 1$, while the perturbation generates the small amplitude b of the opposite spin. The spin mixing parameter $b_{n,\mathbf{k}}^2$ is defined as⁷¹:

$$b_{n,\mathbf{k}}^2 = \int_{\text{u.c.}} |b_{n,\mathbf{k}}(\mathbf{r})|^2 d\mathbf{r}, \quad (2)$$

in which the integration runs over the entire unit cell.

As $\psi_{n,\mathbf{k}}^\uparrow(\mathbf{r})$ and $\psi_{n,\mathbf{k}}^\downarrow(\mathbf{r})$ are degenerate, their linear combination is a valid eigenstate. This arbitrariness is removed by specifying the spin quantization axis (SQA), which could be the orientation of an applied magnetic field or the direction of the injected spin polarization. Say, SQA is given by unit vector $\hat{\mathbf{s}}$. Then, states $\psi_{n,\mathbf{k},\hat{\mathbf{s}}}^\sigma$, $\sigma = \{\uparrow, \downarrow\}$, diagonalize the spin one-half operator $\mathbf{S} \cdot \hat{\mathbf{s}}$, in which $\mathbf{S} = \frac{\hbar}{2}\boldsymbol{\sigma}$. For instance, if $\hat{\mathbf{s}} = \hat{\mathbf{x}}$, then $|\uparrow\rangle$ and $|\downarrow\rangle$ are eigenstates of $S_x - \sigma_x$, that is, $|\uparrow\rangle_x$ and $|\downarrow\rangle_x$, and the spin expectation value $\langle\psi_{n,\mathbf{k},\hat{\mathbf{s}}}^\uparrow|S_x|\psi_{n,\mathbf{k},\hat{\mathbf{s}}}^\uparrow\rangle$ is maximal. At the same time, matrix elements $\langle\psi_{n,\mathbf{k},\hat{\mathbf{s}}}^\uparrow|S_y|\psi_{n,\mathbf{k},\hat{\mathbf{s}}}^\uparrow\rangle = \langle\psi_{n,\mathbf{k},\hat{\mathbf{s}}}^\uparrow|S_z|\psi_{n,\mathbf{k},\hat{\mathbf{s}}}^\uparrow\rangle = 0$. For a given SQA, the spin mixing parameter can also be expressed as a deviation of the spin expectation value from its nominal value 0.5 (ref. 71):

$$b_{n,\mathbf{k},\hat{\mathbf{s}}}^2 = \frac{1}{2} - \frac{1}{\hbar} \langle\psi_{n,\mathbf{k},\hat{\mathbf{s}}}^\sigma|S_{\hat{\mathbf{s}}}|\psi_{n,\mathbf{k},\hat{\mathbf{s}}}^\sigma\rangle. \quad (3)$$

For normalized states $0 \leq b_{n,\mathbf{k},\hat{\mathbf{s}}}^2 \leq 0.5$, in which $b_{n,\mathbf{k},\hat{\mathbf{s}}}^2 = 0.5$ corresponds to the fully spin mixed states, that is, $|a_{n,\mathbf{k},\hat{\mathbf{s}}}(\mathbf{r})| = |b_{n,\mathbf{k},\hat{\mathbf{s}}}(\mathbf{r})|$, whereas for $b_{n,\mathbf{k},\hat{\mathbf{s}}}^2 = 0$ the states (1) are pure Pauli spinors.

As the spin mixing parameter is calculated from the wavefunctions containing information about crystal symmetry and orbital band composition, it can be highly anisotropic reflecting the symmetry of the crystal^{71–73}. This makes the spin mixing parameter very practical, for instance, in the search for type II Ising superconductors⁷⁴. Similar to type I Ising superconductors, they exhibit resilience against strong magnetic fields owing to strong SOC; however, unlike their type I counterparts, they retain inversion symmetry⁷⁵ (for example, in few-layer stanene⁷⁶). Instead of spin–momentum locking which protects type I Ising pairing, type II Ising pairing is protected by spin-orbital locking, which can be uncovered by anisotropy of spin admixture b^2 .

The calculation of $b_{n,\mathbf{k},\hat{\mathbf{s}}}^2$ by DFT codes requires access to the Kohn–Sham eigenstates. Using a pair of degenerate Bloch states as the basis set, one diagonalizes the operator $\mathbf{S} \cdot \hat{\mathbf{s}}$ to find the spin expectation values of this projected spin operator. Alternatively, one can apply an

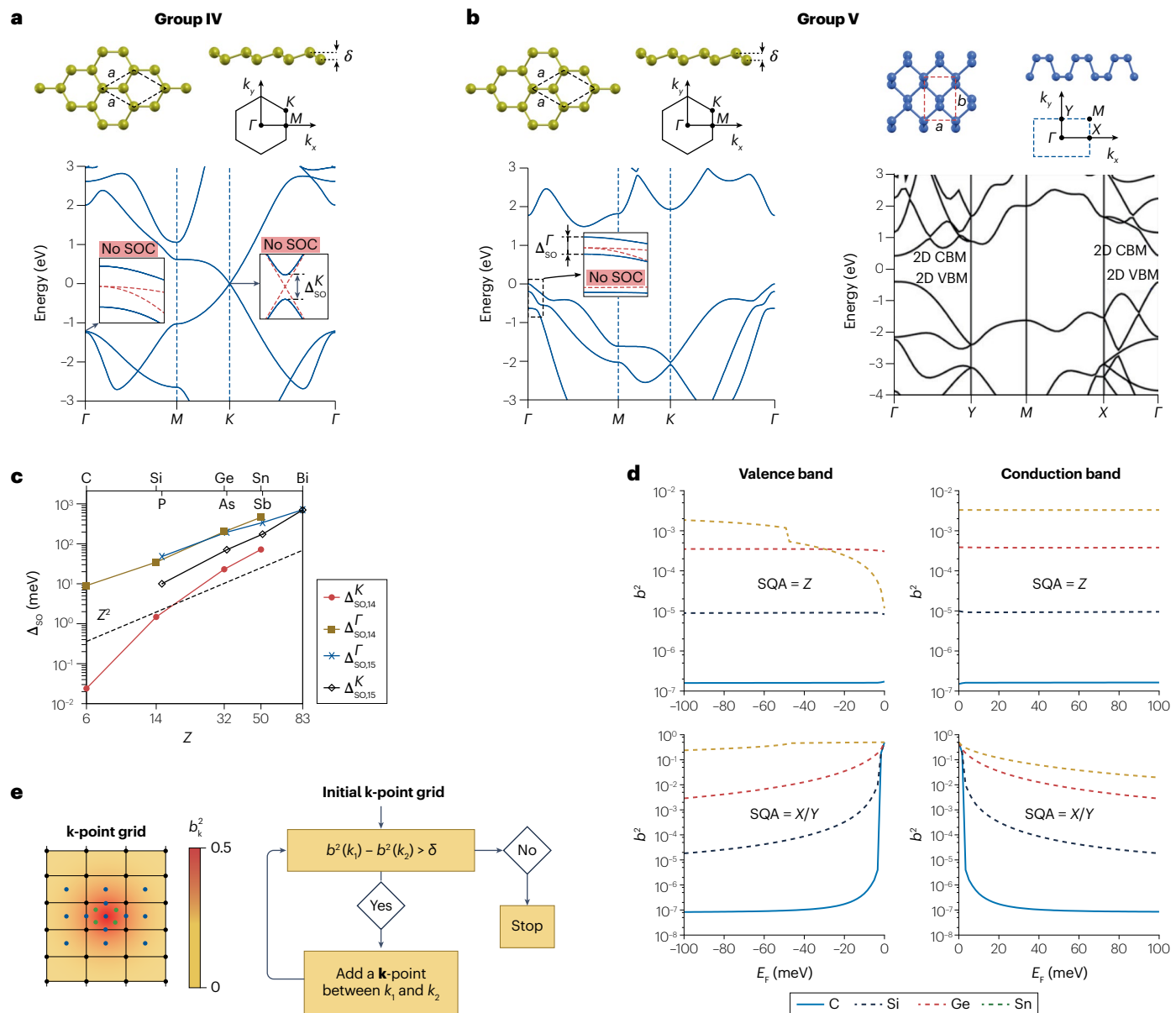


Fig. 2 | Spin-orbit coupling in group IV and group V elemental 2D materials.

a, Top: crystalline structure of buckled group IV monolayers with the unit cell of length a indicated by a dashed line, the buckling height δ and the corresponding Brillouin zone. Bottom: relativistic electronic band structures of silicene plotted along high symmetry lines of the Brillouin zone. The insets show orbital split-offs at high symmetry points owing to spin-orbit coupling (SOC). **b**, Crystalline structure and the corresponding Brillouin zone of buckled (left) and puckered (right) group V 2D materials. Bottom: the electronic band structure for buckled monolayer arsenic and puckered black phosphorus. The conduction-band minima (CBM) and valence-band maxima (VBM) are indicated. **c**, Spin-orbital splittings at the Γ ($\Delta_{\text{SO}}^{\Gamma}$)

and K (Δ_{SO}^K) points from first-principles calculations for group IV ($\Delta_{\text{SO}}^{\Gamma/K}$) and group V ($\Delta_{\text{SO}}^{\Gamma/K}$) 2D materials plotted against the atomic number Z indicating Z^2 dependence of SOC. See Table 1 for the tabulated values. **d**, Average spin-mixing parameter b^2 versus the Fermi energy relative to the valence (conduction) band maximum (minimum) for group IV materials labelled by the element name.

e, A schematic of the adaptive grid method. New \mathbf{k} -points are added to the grid until the condition $|b^2(k_i) - b^2(k_j)| > \delta$ is false for all \mathbf{k} -points from the mesh, and δ is a small positive real number. SQA, spin quantization axis. Panels **a**, **c**, **d** and the left column of panel **b** are adapted with permission from ref. 56, APS. The band structure in the right column of panel **b** is adapted with permission from ref. 158, ACS.

infinitesimal (numerically small) external magnetic field \mathbf{B} in the direction of $\hat{\mathbf{s}}$, which couples to the electron spins via Zeeman coupling. The field breaks the spin symmetry and sets the SQA along $\hat{\mathbf{s}}$. There is then no need to diagonalize the projected spin operator, and $b_{n,\mathbf{k},\hat{\mathbf{s}}}^2$ can be calculated using the formula (3).

Experimentally, the spin mixing parameter can be extracted from the non-local Hanle spin-injection measurements⁵³. If spin relaxation is dominated by the Elliott–Yafet mechanism^{57,77}, the spin relaxation rate (inverse of spin relaxation time) $1/\tau_s$ can be obtained from the momentum relaxation rate $1/\tau_p$ as⁷²: $\tau_s^{-1} \approx ab^2\tau_p^{-1}$, in which b^2 is the Fermi

surface average of $b_{n,k,s}^2$ and α is an empirical parameter typically between 1 and 10.

As $b_{n,k}^2$ can vary widely across the Brillouin zone, it is advisable to use accurate integration methods for obtaining b^2 . One example is the tetrahedron method⁷⁸, whose linear interpolation procedure reduces the need for a fine k -mesh. Still, if the Fermi contour is irregular or small, say one is close to the K -point in 2D semimetals, or in regions where $b^2 \approx 0.5$, and adaptive refinement of the k -point mesh may be necessary, see Fig. 2e.

If SOC can be treated as a perturbation, $b_{n,k,s}^2$ is small, on the order of $(\lambda_{so}/E_F)^2$, in which λ is the strength of SOC and E_F is the Fermi energy⁷² (see Fig. 2d for SQA = Z and SQA = X/Y for $|E_F| > 40$ meV). However, at spin hot spots⁷², which are SOC-induced anticrossings, see insets in Fig. 2a,b, $b_{n,k,s}^2$ can reach its maximal value of 0.5 (full spin-mixed states). For 2D honeycomb materials, spin hot spots are at K or Γ points, see Fig. 2d for $E_F \rightarrow 0$ (ref. 56).

2D solids with broken space-inversion symmetry

Non-centrosymmetric solids exhibit spin-split bands owing to the presence of SOC. Although Kramer's degeneracy is still present, states with the same momentum but opposite spins no longer have the same energy: $E(\mathbf{k}, \uparrow) \neq E(\mathbf{k}, \downarrow)$. Spin degeneracy is still present at the 'time-reversal invariant momenta', whose time-reversed partners are connected by a reciprocal lattice translation; for example, Γ and M points in a hexagonal lattice.

Perhaps, the most representative group of 2D non-centrosymmetric materials are transition-metal dichalcogenides (TMDCs), which can host various interesting phenomena, such as topology, superconductivity and charge density waves (CDWs)⁷⁹ (Fig. 3). TMDCs are also appealing for their fascinating light–matter interactions, exemplified by the presence of excitonic quasiparticles (bound electron–hole pairs) with large binding energies of a few hundred millielectronvolts⁸⁰. A monolayer TMDC comprises three atomic layers, a metal layer (Mo, W, Pt, Nb, Ta) sandwiched by two chalcogen atoms (S, Se, Te). In addition, the different arrangements of the chalcogen atoms with respect to the metal atoms lead to very different electronic properties.

In the H-phase, the chalcogen atoms have a trigonal prismatic arrangement, such that the metal atom layer forms a horizontal mirror plane. The presence of a mirror plane enforces perpendicular spin orientation for Bloch states. Although H-type monolayers lack inversion symmetry, in bilayers it is restored. H-phase TMDCs are semiconductors, with band gaps in the range of around 2 eV (ref. 81). A monolayer has a direct gap at the K/K' valleys, and a few layers an indirect one.

In the T-phase, the chalcogen atoms have an octahedral arrangement, such that a metal atom acts as an inversion centre. Therefore, a monolayer TMDC in the T-phase has inversion symmetry and the electronic bands are spin degenerate. Typically, TMDCs in this phase are metals. There is also a T' -phase, in which the threefold symmetry is broken and the lattice is distorted, forming an orthorhombic crystal structure. The transition from H or T to T' occurs spontaneously, but it can also be driven by straining or gating, accompanied by a topological phase transition⁸². In the bulk one distinguishes T' , T_d and T_d^* phases from the stacking order of the monolayers.

SOC in monolayer TMDCs is relatively strong, leading to the prominent splitting of the conduction and valence bands⁸³ in the H-phase (Fig. 3). Note the subtle differences between the spin-split conduction band structure of Mo-based and W-based TMDCs. The valence band edge is split by hundreds of millielectronvolts, whereas the conduction band edge by a few to tens of millielectronvolts. Owing to the presence

of the horizontal mirror plane, the spin–orbit fields around the band extrema are locked to the out-of-plane direction, opposite in K and K' ; hence the term spin-valley locking. This strong interplay between the valley and spin degrees of freedom can be exploited in highly efficient optical orientation, that is, the excitation of the electron and hole spins by circularly polarized light⁸¹.

The energy dispersions of H-type monolayer TMDCs have been described by tight-binding models comprising transition-metal d -orbitals and chalcogen p -orbitals⁸³. The low energy band edges in the vicinity of the K points, including the effects of SOC, can be described by the relatively simple massive Dirac Hamiltonian⁸¹:

$$\mathcal{H} = \hbar v_F s_0 (\tau \sigma_x k_x + \sigma_y k_y) + \frac{\Delta}{2} s_0 \sigma_z + \tau s_z (\lambda_c \sigma_+ + \lambda_v \sigma_-). \quad (4)$$

The orbital basis spans the wavefunctions $|\Psi_c\rangle = |d_{z^2}\rangle$ and $|\Psi_v\rangle = \frac{1}{\sqrt{2}}(|d_{x^2-y^2}\rangle + i\tau|d_{xy}\rangle)$, corresponding to the conduction (c) and valence (v) band edges at K ($\tau = 1$) and K' ($\tau = -1$), which are formed by different d -orbitals of the transition metal atoms⁸³. v_F is the Fermi velocity and k_x and k_y are the Cartesian wave vector components, measured from K (K'). The pseudospin Pauli matrices σ_i act on the (c,v) subspace, whereas spin Pauli matrices s_i act on the spinors (\uparrow, \downarrow), with $i = \{0, x, y, z\}$ and $\sigma_{\pm} = \frac{1}{2}(\sigma_0 \pm \sigma_z)$. H-type TMDCs are semiconductors and the orbital gap is represented by the parameter Δ . Thus, the first two terms in the Hamiltonian describe a gapped spectrum with spin-degenerate parabolic conduction and valence bands. The bands are spin split owing to SOC, which is captured by the last term with the parameters λ_c and λ_v describing the spin splitting of conduction and valence bands. Specific values for the spin–orbit splittings of conduction (valence) band edges at K of semiconducting H-type MoS₂, MoSe₂, WS₂ and WSe₂ are in the range of 3–40 (149–466) meV. For a more detailed and extended list of values, comparing also experimental and GW results, see ref. 83. The SOC terms are proportional to $s_z \sigma_0$ and $s_z \sigma_z$, which are akin to Kane–Mele and valley–Zeeman SOC terms in (proximitized) graphene (Box 1). The SOC term together with broken inversion symmetry is responsible for the spin-valley locking in semiconducting TMDCs⁸¹.

Table 1 | Spin–orbit gaps at high symmetry points Γ and K of the Brillouin zone of elemental 2D buckled honeycomb lattice materials from first-principles calculations using the Perdew–Burke–Ernzerhof Generalized Gradient Approximation (PBE GGA) exchange–correlation functional⁵⁶

Material	Group	$\frac{\Delta_{so}^K}{\text{(meV)}}$	$\frac{\Delta_{so}^\Gamma}{\text{(meV)}}$
Graphene	IV	0.024	9
Silicene	IV	1.48	34.6
Germanene	IV	23	201
Stanene	IV	72	461
Plumbene	IV	470	
Blue phosphorus	V	10	48
Arsenene	V	71	195
Antimonene	V	174	340
Bismuthene	V	702	712

The value for plumbene was calculated using the local-density approximation exchange–correlation functional, taken from ref. 157.

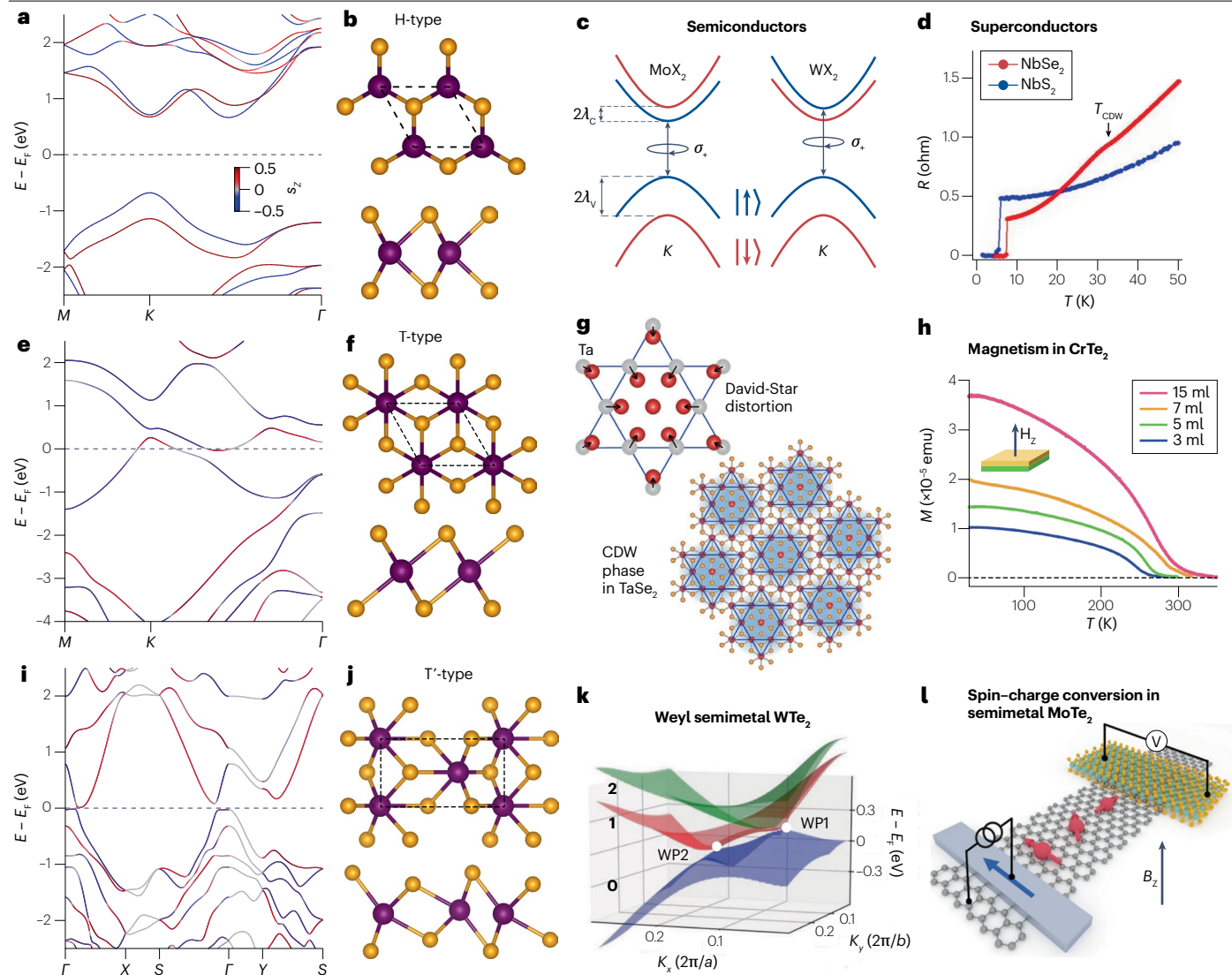


Fig. 3 | Overview on the different transition-metal dichalcogenide polytypes (H, T, T') with a vast variety of physical properties and phenomena. For each polytype, we show in panels **a**, **e** and **i** an exemplary band structure of WSe_2 in that polytype, as well as in panels **b**, **f** and **j** a top and side view of the geometry. Depending on the polytype and the involved atomic constituents, very different electronic, magnetic, topological and more exotic phases can arise. **c**, MoX_2 and WX_2 , with $\text{X} = \text{S}, \text{Se}$, are semiconductors in the H-phase, feature spin-valley locking and have highly interesting optical properties. **d**, By contrast, NbS_2 and NbSe_2 in the H-phase are metallic superconductors. **g**, A charge density wave (CDW) phase. **h**, Considering CrTe_2 in the T-phase, magnetism with perpendicular magnetic

anisotropy arises for ultrathin samples. For TaSe_2 and NbSe_2 in the T-phase, a robust CDW phase – star of David distortion – is present, stemming from electron correlations and electron–phonon coupling. Non-trivial topological states arise in WTe_2 and MoTe_2 in the T'-phase. **k**, **l** Both materials are Weyl semimetals, exhibiting unconventional multidirectional spin–charge conversion. Panel **c** adapted with permission from ref. 159, APS. Panel **d** adapted with permission from ref. 160, AAAS. Panel **g** is adapted from ref. 161, CC BY 4.0. Panel **h** is adapted from ref. 162, CC BY 4.0. Panel **k** is adapted from ref. 163, CC BY 4.0. Panel **l** is adapted with permission from ref. 147, ACS.

A special group of TMDCs consists of metallic systems that exhibit spontaneous symmetry breaking owing to enhanced electron–phonon coupling. This interaction leads to periodic lattice distortions and the formation of a CDW phase⁸⁴ (Fig. 3). The phase transition to commensurate CDW is around 200 K for TiSe_2 (ref. 85), 180 K for TaS_2 (ref. 86) and 33 K for NbSe_2 (ref. 87). Another complexity observed in the CDW phase is the emergence of chiral and orbital charge order in 1T- TiSe_2 (refs. 88–91), 1T- TaS_2 (refs. 92,93) and 2H- NbSe_2 (ref. 94),

breaking threefold symmetry. It has been shown that CDW remains intact down to monolayer limit in 2H- NbSe_2 along with the existence of superconductivity^{95,96}. Proximity effects on CDW and superconductivity in the monolayer 1H- NbSe_2 on different substrates show disparate behaviours⁹⁷. There have been several attempts to unveil correlations between the CDW and superconductivity such as introducing Cooper-pair density wave concept⁹⁸ or studying superfluid density scaling probed by muon spin rotation⁹⁹. The strong Ising spin–orbit

fields in superconducting TMDCs make the superconducting order resilient to the application of an in-plane magnetic field^{100,101}, leading to type-I Ising pairing.

Finally, TMDCs in the T'-phase exhibit non-trivial band-structure topologies driven by SOC as illustrated in Fig. 3. For example, a single layer of 1T'-WSe₂ shows a large quantum spin Hall gap accompanied by in-gap edge states¹⁰². Similarly, bulk T'-phase MoTe₂ and WTe₂ exhibit a type-II Weyl semimetal phase, in which Weyl points break Lorentz symmetry^{103,104}, whereas the monolayers also feature quantum spin Hall states^{105,106}.

Often, realistic models are necessary to identify topological properties of materials such as TMDCs or to perform large-scale quantum transport calculations. One effective method is to construct maximally localized Wannier functions from the Bloch states, resulting in a numerical tight-binding model implemented by Wannier90 code¹⁰⁷. With the Wannier Hamiltonian, one can calculate electric, spin and phonon transport; Berry curvature; spin and anomalous Hall conductivity; and other topological properties of the system^{107–109}.

Proximity effects in 2D heterostructures

Early DFT investigations of graphene and semiconducting TMDC bilayers found that the Dirac states of graphene are nicely preserved within the TMDC band gap¹¹⁰. Zooming in on the low-energy bands at the Fermi level reveals that the Dirac states are spin split by ~1 meV. This is significantly larger than the intrinsic SOC of graphene, which is on the order of 10 µeV (refs. 52,111). This induced splitting stems from the proximity

coupling: the electron wavefunctions hybridize across the van der Waals (vdW) gap and both layers acquire some properties of the other material. Remarkably, even though TMDC orbitals contribute only about 1% to the graphene *p_z* bands at K, this hybridization is sufficient to yield millielectronvolt-strong proximity SOC of the Dirac electrons. However, not only the value of SOC is significantly increased but also spin–orbit fields acquire a new functional form. Instead of the Kane–Mele type, the proximity-induced SOC is of the valley–Zeeman (also called Ising SOC, as in TMDCs) type^{52,111}. However, one can still engineer Kane–Mele SOC, for example, by considering bilayer graphene (BLG) encapsulated by WSe₂, stacked such that the valley–Zeeman coupling is opposite in the two graphene layers¹¹². This would be important for creating helical states. Naturally, as the horizontal mirror symmetry is broken, Rashba coupling also emerges. In Box 1, we give the Hamiltonian description, used for phenomenological modelling, of the low-energy bands in proximitized graphene. In Box 2, we summarize the corresponding band structure topologies that result from this emergent Hamiltonian.

Different TMDCs induce varying degrees of proximity SOC. Once SOC exceeds the orbital gap, one can tune the Dirac bands into an inverted regime, as in the case of untwisted graphene/WSe₂ (ref. 113) or graphene proximitized by alloyed TMDC¹¹⁴. What is the spatial range of the proximity effects? It appears that hybridization is significant only for the adjacent layers, so the proximity effects are extremely short-ranged, diminishing exponentially beyond the nearest layers¹¹⁵. It is then often sufficient to study hetero-bilayers by DFT to extract reliable information about proximity-induced SOC in few-layer

Box 1 | Emergent Hamiltonian of proximitized graphene

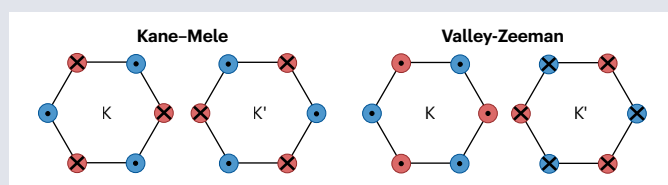
Graphene is the prototype material for proximity effects as the relevant *p_z* orbitals are predestined to hybridize with orbitals from another layer and spin interactions can be induced from other 2D materials. The low-energy bands of (proximitized) graphene in the vicinity of the charge-neutrality point (Dirac point) can be modelled with the effective Hamiltonian considering *p_z* orbitals only¹⁶⁴:

$$H = H_{\text{orb}} + H_{\text{so}}, \quad (5)$$

$$H_{\text{orb}} = \hbar v_F (\kappa \sigma_x k_x + \sigma_y k_y) + \Delta \sigma_z, \quad (6)$$

$$H_{\text{so}} = \lambda_{\text{KM}} \kappa \sigma_z s_z + \lambda_{\text{VZ}} \kappa \sigma_0 s_z + \lambda_{\text{R}} e^{-i\phi_{\text{R}} s_z / 2} (\kappa \sigma_x s_y + \sigma_y s_x) e^{i\phi_{\text{R}} s_z / 2}. \quad (7)$$

The above Hamiltonian, *H*, has orbital and spin-orbital parts. The orbital part, *H_{orb}*, describes gapped Dirac states, in which *v_F* is the Fermi velocity of Dirac electrons, *Δ* is the staggered potential (gap), *σ* are the pseudospin Pauli matrices operating on the sublattice A and B space and *k_x* and *k_y* are the Cartesian components of the electron wave vector measured from K (K'); parameter *κ* = 1 (−1) for K (K'). The spin–orbit Hamiltonian *H_{so}* consists of a Kane–Mele, a valley–Zeeman (Ising) and a Rashba term. The Kane–Mele (or McClure–Yafet–Kane–Mele) term is also called intrinsic SOC, as it describes pristine graphene^{40,165}. However, Dirac states in graphene on 2D spin–orbit material substrates are mostly valley–Zeeman-like. The real space



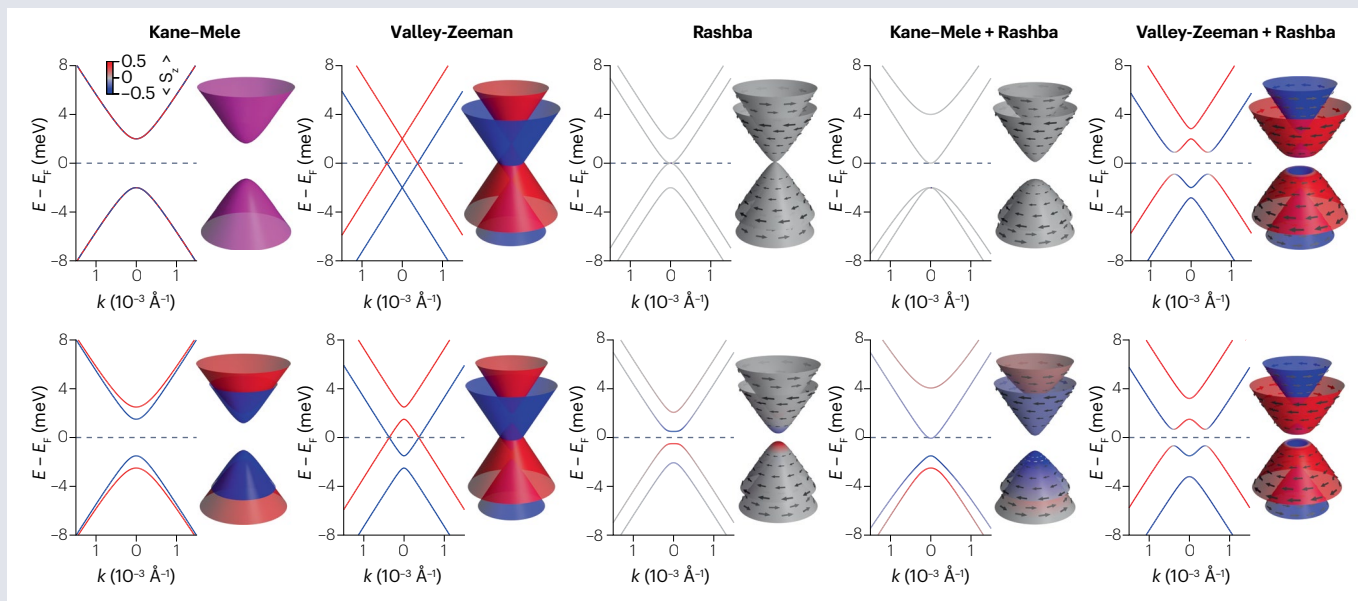
representation of the Kane–Mele and valley–Zeeman spin–orbit fields is shown in the figure. Only recently, the Rashba spin–orbit coupling (SOC) term^{40,166} has been extended to the more general form of the induced Rashba SOC term in twisted graphene/TMDC heterostructures that obeys time reversal, and threefold rotation *C₃* symmetries^{127,128} can be written as *U**H_R**U*, in which *U* = *e*^{−*i**s_z**φ_R*/2}. The Rashba angle *φ_R* originates from SOC matrix elements between *d*-orbitals of metal atoms in TMDC¹²⁷ and, in general, represents a sum of the geometric angle and the quantum phase¹⁶⁷. The Rashba angle represents an important ingredient for the collinear Rashba–Edelstein effect used in charge-to-spin interconversion¹³¹. It turned out that the emergence of the CDW phase in 1T-TaS₂ significantly triggers Rashba angle in proximitized graphene allowing to propose twistrionic devices without twist^{168,169}. Depending on the surrounding materials, very different band structure topologies can arise, depending on the actual parameter values (Box 2).}

Box Fig. 1 | Real space representation of Kane–Mele and valley–Zeeman spin–orbit fields. The red and blue spheres represent the A and B sublattice of graphene, whereas the dot and the cross represent the direction of the spin–orbit field (out-of-plane). Owing to *κσ_z*, Kane–Mele spin–orbit field is alternating on the sublattices and is opposite for the valleys. Owing to *κσ₀s_z*, valley–Zeeman spin–orbit field is even for the sublattices but opposite for the valleys.

Box 2 | Band structure topologies of proximitized graphene

In Box 1, we show the effect of the different Hamiltonian terms on the low-energy Dirac bands in proximitized graphene. Here, we show a 3D surface plot and a line-cut for five types of spin-orbit coupling. The colour code (red and blue) represents the out-of-plane spin, whereas in-plane spins (if present) are visualized with arrows. Grey means no significant out-of-plane spin, and pink (Kane–Mele case with $\Delta = 0$)

means spin degenerate bands. In all figures, we use $v_F = 8 \times 10^5 \text{ ms}^{-1}$. For Kane–Mele (KM), valley-Zeeman and Rashba spin-orbit coupling, we use $\lambda_{\text{KM}} = 2 \text{ meV}$, $\lambda_{\text{VZ}} = 2 \text{ meV}$ and $\lambda_{\text{R}} = 1 \text{ meV}$. In the upper (lower) row, we use a staggered potential of $\Delta = 0$ ($\Delta = 0.5 \text{ meV}$). White arrows in the surface plot of the KM + Rashba + Δ indicate the change of in-plane spin texture at $\sim 1 \text{ meV}$ below the valence band maximum.



heterostructures. For example, to model BLG in proximity with a thin layer of WSe_2 , one can take the hopping Hamiltonian of BLG¹¹⁶ and add the proximity SOC Hamiltonian terms only to the layer in contact with WSe_2 . Such a Hamiltonian faithfully describes the proximity BLG even in the presence of displacement field^{117,118}.

The ‘Hamiltonian discovery’, meaning the introduction of an effective few-orbital Hamiltonian describing the relevant physics, is a beautiful example of the potential of DFT when it comes to 2D materials. Considering that the supercells in graphene/TMDC heterostructures contain many atoms, it is noteworthy that the Dirac bands can still be accurately described by a very simple valley-pseudospin-spin Hamiltonian. One needs to carefully consider the supercell spatial symmetries, band dispersions, as well as the spin, pseudospin, valley and perhaps layer character of the bands to design and fit an effective Hamiltonian. We also stress that one needs to zoom in very close to the special symmetry points (such as K or Γ) in DFT-calculated band structures to resolve the sub-millielectronvolt features that could be relevant for obtaining an accurate analytical description of the proximitized bands. The fitting procedure, to obtain the model Hamiltonian parameters from the DFT calculations, is summarized in Box 3.

Engineering spin–orbit coupling

Two-dimensional materials offer significant advantages, in terms of tailoring SOC, over their bulk counterparts owing to the tunability provided by vdW stacking. In Fig. 4, we illustrate the engineering of SOC through twisting, alloying, straining under pressure, lattice mixing

or multilayer stacking. DFT methods, although indispensable to make quantitative predictions for different tuning knobs, entail specific challenges as described next.

Heterostructure setup and the role of strain

The lattice mismatch is the first challenge in stacking two different monolayers. Even when the crystal structures are the same, the lattice parameters are typically not. By contrast, DFT calculations of extended systems rely on periodically repeated commensurate supercells, which are unit cells of the compound structure. To achieve commensurability between the lattice parameters of the constituent monolayers, strain needs to be introduced to keep the supercell sizes computationally manageable (say, up to 1,000 atoms). This artificial strain can significantly modify the electronic band structure. In Box 4, we describe the coincidence lattice method to build commensurate supercells suitable for DFT codes.

Consider bilayers composed of graphene and semiconducting TMDCs. The latter exhibit significant sensitivity of their band gaps, work functions and spin–orbit splittings to biaxial strain^{119,120}. For example, the renormalization of the direct band gap in monolayer H-type TMDCs is on the order of 100 meV for biaxial strain of 1%, accompanied by direct-to-indirect band gap transitions¹¹⁹. Therefore, it is advisable to minimize the strain in TMDCs to avoid strain-related artefacts. However, graphene is susceptible to strain as well; its work function and the Fermi velocity change under biaxial strain^{121,122}. For example, for $\pm 1\%$ of strain, the work-function changes by $\pm 100 \text{ meV}$ (ref. 121). Furthermore, uniaxial strain in

graphene breaks its threefold rotation symmetry. The nearest neighbour atoms become inequivalent and the Dirac point shifts away from K ^{123,124}.

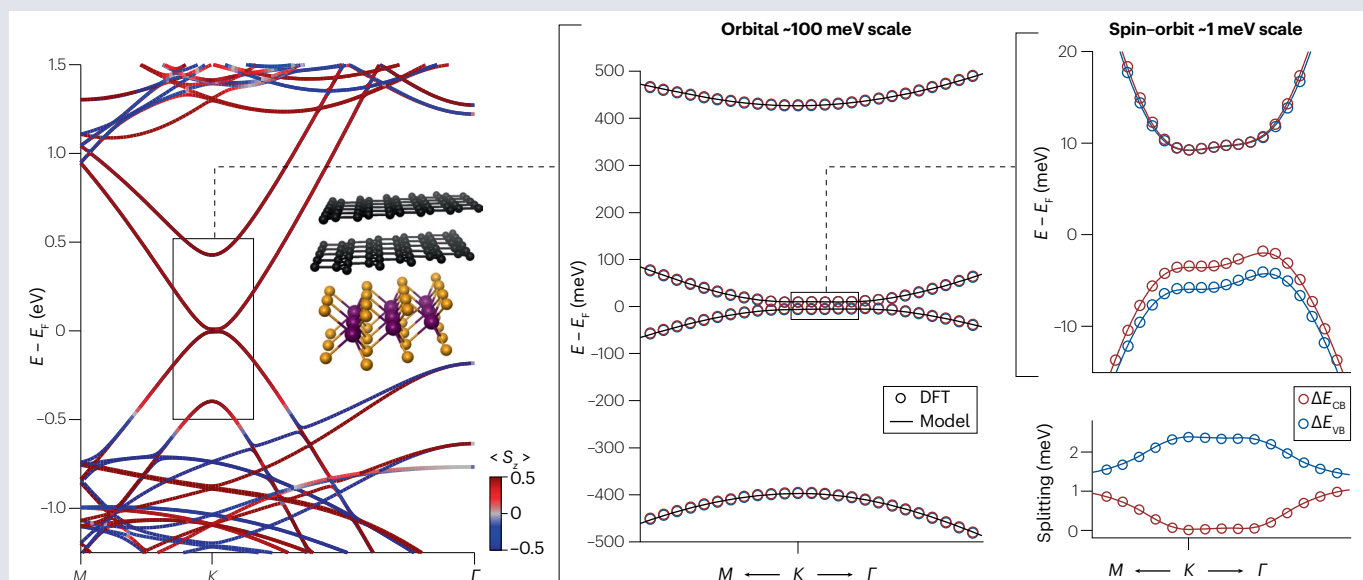
Which layer should be strained in the DFT supercell: graphene, TMDC or both? There is no definitive answer, but selecting supercells with minimal strain, ideally below 1%, is certainly a wise strategy. However, it is important to understand the secondary artefacts that strain can induce. First, strain affects the orbital overlap across the vdW gap, which can affect the proximity effects. Second, owing to the work

function dependence on strain, different in different materials, there will be strain-induced band offsets in the calculated band structures of the bilayers. Indeed, recent systematic studies^{125,126} of graphene/TMDC with unstrained TMDCs and strained graphene have found a linear-in-strain band offset of the Dirac point with respect to the TMDC band edges with tuning rates of around 80 meV per percent. Still, proximity SOC parameters could be reliably extracted even for strains above 1% using corrective displacement fields¹²⁵.

Box 3 | Fitting procedure

How can one reliably extract model Hamiltonian parameters from the first-principles calculated band structure? Certainly, this depends on the number of model parameters and the number of physical quantities that can be calculated for their determination. Under certain assumptions, one can analytically determine them, see, for example, ref. 170, in which proximity spin-orbit coupling (SOC) parameters for graphene on Cu(111) have been extracted in this way. More frequently, a least-squares fitting routine is used, to minimize the sum of the squares of the residuals between model and density functional theory (DFT)-calculated quantities. This routine is implemented in many modern programming languages and libraries^{171–173}. The relevant quantities in the case of proximitized graphene are band energies, splittings and spin-expectation and sublattice-expectation values. Before the actual fitting process, one should familiarize oneself with the adjustable model Hamiltonian parameters. In particular, how is the dispersion affected when tuning different parameters and what are realistic limits for them? Still, the fitting procedure is not a straightforward task, as different energy scales may be present as well. In proximitized monolayer,

bilayer and trilayer graphene, the orbital parameters or hopping amplitudes are typically in the range of hundreds of millielectronvolts to few electronvolts, whereas proximity-induced SOC or exchange parameters are in the range of few microelectronvolts to few millielectronvolts. If many unknown fitting parameters are involved, the strategy is then as follows. Focusing on band energies only, the orbital parameters are determined first by the least-squares routine, setting SOC and exchange parameters to zero. Once the orbital parameters are fixed, we can fit for the remaining parameters, taking into account band splittings and spin expectation values. Sometimes, it may also happen that the model Hamiltonian needs to be adjusted. For example, when the threefold rotation symmetry in graphene is broken, the Dirac point may be shifted in momentum space and direction-dependent nearest neighbour hoppings arise^{123,124}. Similarly, in twisted graphene/transition-metal dichalcogenide heterostructures^{127,128}, a Rashba phase angle can arise or even more complex charge density wave phase proximity effects in graphene/TaS₂ can be seen (ref. 168). In the figure, we illustrate the fitting on the example of a stack of bilayer graphene (BLG) and WSe₂.



Box Fig. 1 Fitting procedure. From left to right: (1) the DFT calculated global band structure of a BLG/WSe₂ heterostructure. The colour code represents the s_z spin expectation value and the inset shows the geometry. (2) Zoom in on the relevant low-energy BLG bands (dashed box in 1) with an orbital fit that reproduces the global band structure features but not splittings nor spins. (3) Zoom in on the fine structure of the low-energy valence band (VB) and conduction band (CB) and their spin splittings. The fit, including orbital and spin-orbit terms (valley-Zeeman and Rashba), reproduces the dispersion, splittings and spins.

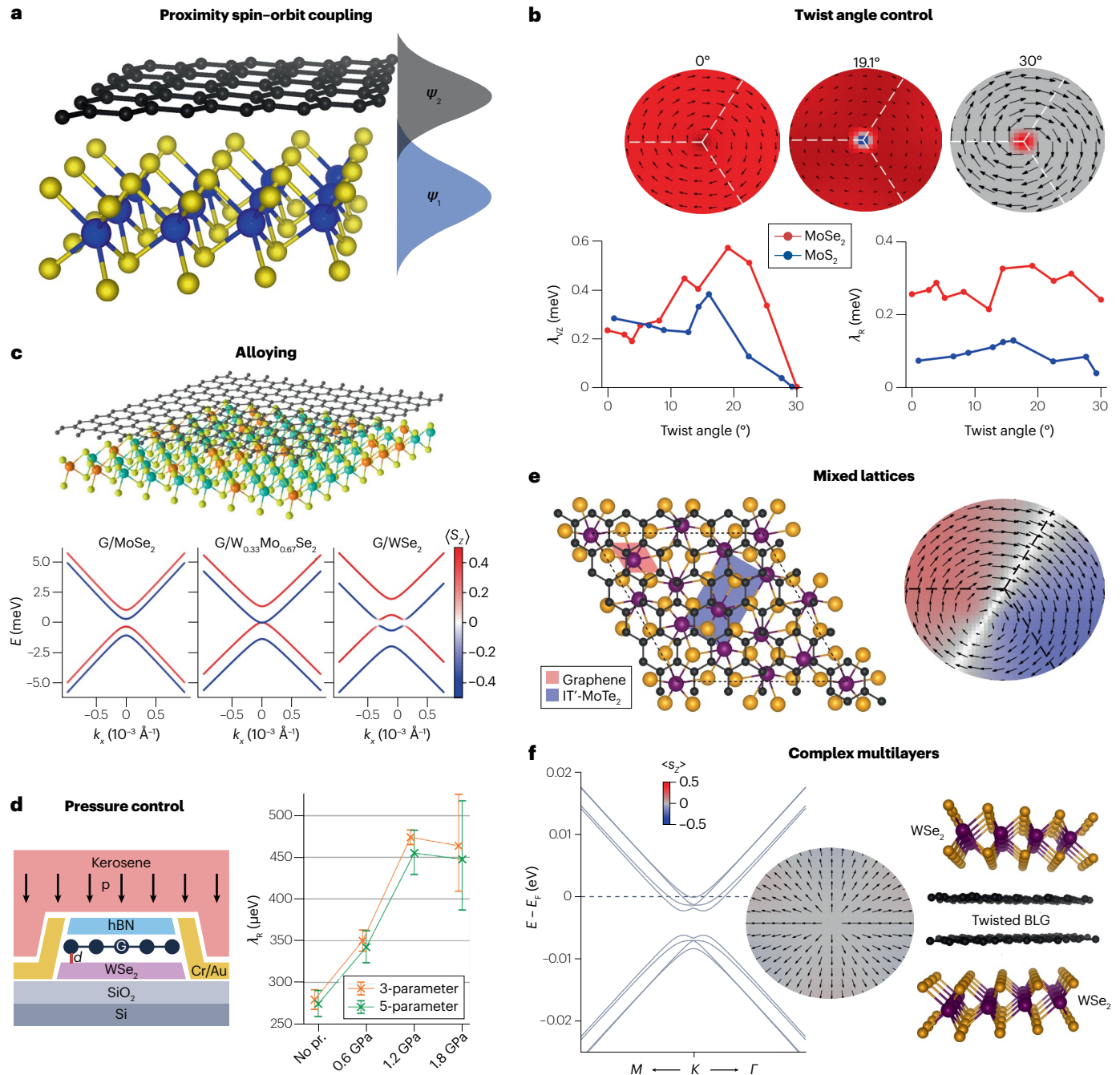


Fig. 4 | Engineering of spin-orbit coupling. **a**, The prototype platform for proximity-induced spin-orbit coupling (SOC) is the graphene/transition-metal dichalcogenide heterostructure, in which the wavefunctions of the individual monolayers overlap and hybridize. **b**, With the twist angle, one can control the proximity valley-Zeeman and Rashba SOC, tuning also the spin-orbit fields. The Rashba coupling, for example, acquires a radial component, for twist angles between 0° and 30°. Note that we plot the in-plane spin-orbit fields as arrows, whereas the colours (red and blue) represent the out-of-plane spin components (grey is unpolarized). **c**, Alloying allows the tuning of the metal composition within the transition-metal dichalcogenide, enabling tailored spin splittings,

shown here for Gr/Mo_{1-x}W_xSe₂. **d**, Applying external pressure will reduce the interlayer distance, thereby enhancing the wavefunction overlap and increasing the proximity SOC. **e**, In mixed lattice structures, such as hexagonal graphene and rectangular IT' MoTe₂, the Dirac point is shifted away from *K* and spin-orbit fields become rather complex. **f**, In twisted multilayer structures, purely radial spin-orbit fields can arise owing to the interference of opposing twisted Rashba fields. BLG, bilayer graphene; hBN, hexagonal boron nitride. Panel **b** adapted with permission from ref. 126, APS. Panel **c** adapted with permission from ref. 114, APS. Panel **d** is adapted from ref. 135, CC BY 4.0. Panel **e** (right) is adapted from ref. 133, CC BY 4.0. Panel **f** adapted with permission from ref. 132, APS.

Twisting

Proximity SOC in graphene/TMDC bilayers is highly sensitive to twisting, as predicted by tight-binding modelling^{127,128}, elaborated on by DFT simulations^{9,125,126,129} and confirmed experimentally¹³⁰, (T. Rockinger and J. Eroms, personal communication). The twist-angle dependence of the proximity effect arises because the Dirac states at K interact with different momenta in the TMDC Brillouin zone for varying twist angles. The full picture can be understood from the perspective of the backfolding of the monolayer Brillouin zones into the common supercell Brillouin zone.

Two important effects can be extracted from the dependence of the proximity spin–orbit effects in graphene on TMDCs. First, the valley–Zeeman coupling disappears for the twist angles of 30° owing to symmetry reasons: the Dirac point of graphene lies exactly in between K and K' of TMDC; they induce opposite spin–orbit fields, cancelling each other out. Second, the Rashba coupling acquires a phase for twist angles between 0° and 30° , resulting in a tilted Rashba spin–orbit field. The Rashba field has thus both tangential (to the momentum) and radial components, resulting in unconventional (collinear) spin–charge conversion¹³¹. In twisted homobilayers, but also multilayers (discussed subsequently), it should be possible to achieve purely radial Rashba spin–orbit fields¹³².

Gating

In experiments, gating is an important tool to control both the charge carrier density and the displacement-field induced proximity effects.

For example, ref. 133 demonstrated that a gate voltage can modify the spin–charge conversion efficiency in graphene/MoTe₂ heterostructures. Similarly, in DFT calculations, one can simulate an electric field perpendicular to the monolayers to investigate proximity effects¹²⁶. The electric field provides an electrostatic potential difference across the bilayer, shifting the Dirac states within the TMDC band gap. Furthermore, an electric field enhances the inversion symmetry breaking, affecting the Rashba coupling. In the case of hybridizing bands, the electric field can even shift the Dirac states through a resonant band anticrossing, thereby massively tuning, enhancing or even inverting Dirac band spin splittings¹³⁴.

Pressure

Recent experiments have shown that one can also tune proximity SOC by external pressure, thereby reducing the interlayer distance between graphene and the TMDC^{135,136}. In particular, by applying external pressure of about 1.8 GPa to a graphene/WSe₂ heterostructure and diminishing the interlayer distance by about 9% leads to a twofold enhancement of the proximity-induced Rashba SOC, as found by magnetotransport experiments¹³⁵. With DFT calculations, external pressure can be simulated by a rigid interlayer distance reduction. When decreasing the distance between the layers, the wavefunctions overlap across the vdW gap and thus the proximity SOC increases¹³⁵.

First-principles calculations of graphene/TMDC bilayers have shown that the proximity-induced SOC can be increased by a factor of 2–3, when

Box 4 | Coincidence lattice method

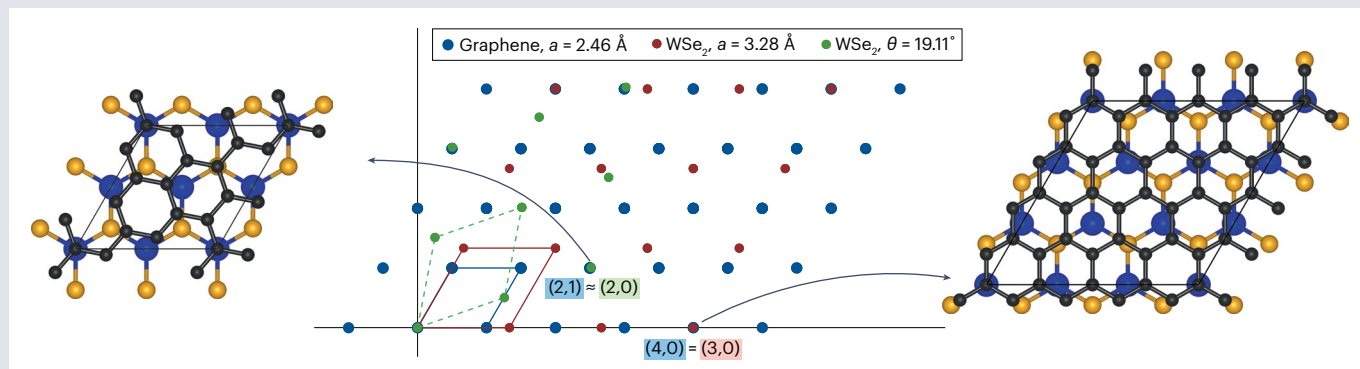
To calculate the electronic and spin properties of van der Waals heterostructures from first principles, it is inevitable to initially combine individual monolayers into a commensurate periodic supercell. In some rare cases, this may be possible, for example, when combining hexagonal lattices, such as graphene and transition-metal dichalcogenides, at 0° . However, in most cases, one needs to rely on the coincidence lattice method which goes as follows^{174,175}: we start from the Bravais lattices of two different 2D materials A and B:

$\mathbf{R}_A = n_1 \mathbf{a}_1 + n_2 \mathbf{a}_2$ and $\mathbf{R}_B = m_1 \mathbf{b}_1 + m_2 \mathbf{b}_2$, in which \mathbf{a}_i and \mathbf{b}_i are the primitive lattice vectors of the monolayers and $n_i, m_i \in \mathbb{Z}$ with $i = 1, 2$. One then has to find supercell vectors such that $\mathbf{R}_A = \mathbf{R}_B$, avoiding the null vector. This would lead to an ideal heterostructure supercell without strain;

a condition which is barely fulfilled given two different monolayer lattices. Therefore, we have $\mathbf{R}_A \approx \mathbf{R}_B$ and compensate the difference by straining one of the materials (or both, see the main text). Note that the strain can significantly modify the electronic properties of the monolayers, such that one should avoid straining above a certain threshold, typically ~1–3%, depending on the materials.

We illustrate this procedure in the figure, in which we construct heterostructure supercells of graphene and WSe₂, with and without a twist angle between the monolayers.

Practical tools to setup van der Waals heterostructures are the Atomic Simulation Environment¹⁷⁶ and the CellMatch code¹⁷⁴.



Box Fig. 1 | Coincidence lattice method: the Bravais lattice corresponding to graphene (blue), WSe₂ (red) and twisted WSe₂ (green). By coincidence, the lattice point (4,0) of graphene matches the (3,0) one of WSe₂. Similarly, the lattice point (2,1) of graphene approximately matches the (2,0) one of twisted WSe₂. The corresponding graphene/WSe₂ heterostructures result from the coincidence lattice matching.

reducing the distance by only about 10%, in agreement with experimental findings^{126,136}. In general, proximity effects show an exponential interlayer distance dependency, which can be easily understood by considering the proximity interaction as a Slater–Koster hopping amplitude.

When investigating proximity effects in bilayers through DFT simulations, it is crucial to examine the dependence of the induced SOC on the interlayer distance. The lowest energy interlayer spacing can vary significantly depending on the employed vdW correction. The calculated (equilibrium) spacing thus need not reflect the experimental conditions.

Mixed lattice structures

An important method for engineering SOC in vdW heterostructures is to make mixed (hybrid)-lattice structures, where symmetry breaking results in highly anisotropic spin–orbit fields.

A prototypical example would be graphene/1T′-MoTe₂, combining a hexagonal and a rectangular lattice¹³³. Constructing a commensurate low-strain supercell is already a non-trivial task, as the coincidence lattice method may fail to yield heterostructures of computationally manageable sizes. Furthermore, the threefold rotation symmetry of graphene is explicitly broken and Dirac points are shifted away from *K*. In effective modelling, this shift can be captured by allowing non-uniform nearest neighbour hopping amplitudes^{123,124,137}. Another class of materials suitable for proximitizing graphene are ferroelectric monolayers such as SnTe, capable of inducing giant (15 meV) anisotropic proximity SOC of Dirac bands¹³⁸.

Interplay of spin–orbit and exchange coupling

Two spin interactions are relevant for spintronics with 2D materials: SOC^{112,126,130,139–148} and exchange coupling^{118,149–154}. The latter appears in magnetic materials and can be proximitized to generate 2D synthetic magnets. For example, graphene or a TMDC placed on a ferromagnetic semiconductor such as Cr₂Ge₂Te₆ or CrI₃ would exhibit exchange splittings in their band structures.

Consider graphene on Cr₂Ge₂Te₆ (refs. 155,156). In a DFT simulation, after building a supercell, one initiates a collinear spin-polarized calculation. The finite magnetic moment breaks time-reversal symmetry and Dirac states at *K* are Zeeman-split, typically by 1–10 meV. Similar to SOC, also proximity exchange splitting can be tuned by twisting, straining and so forth. For example, the proximity-induced spin polarization of Dirac bands in graphene/Cr₂Ge₂Te₆ bilayers can be fully reversed upon twisting¹⁵⁵.

Combined effects of proximity exchange (ex) and spin–orbit (so) coupling become important in ‘ex-so-tic’ heterostructures¹¹⁷. One particular example is graphene or BLG encapsulated by WSe₂ and Cr₂Ge₂Te₆ (refs. 117,156). In such heterostructures, it is possible to swap the two spin interactions by applying a displacement field or gate-induced doping.

Conclusion and outlook

We are still early in exploring the proximity effects in vdW materials. We know that spin interactions, in particular SOC, are highly sensitive to stacking variations, involving strain and twist, and to gating, which induces displacement field. Many open questions, which pose challenges for DFT modelling, remain: what is the landscape of proximity-induced SOC in low-strain large-scale heterostructures? Why is the description of relevant physics in systems containing a large number of atoms (large supercells) using only a few degrees of freedom (pseudospin, spin, valley and so on) so effective? What spin–orbit field textures are possible to engineer with complex heterostructures?

Then, there is the whole unexplored area of the interplay of proximity SOC and other interactions, such as electron correlations, electron–phonon coupling and, in particular, exchange coupling. Indeed, the effects of proximity SOC on magnetism can be profound for both fundamental physics and applications. Think of magnetoanisotropies, the anomalous Hall effects, spin–orbit torque, skyrmions or magnetoelectric effects. They can be used to write or read spin-based information.

Discoveries of 2D materials open exciting avenues for engineered spin-based functionalities. DFT is a powerful tool to explore novel spin phenomena and guide the design of materials with tailored spin properties. But it has to be used with caution.

Published online: 25 March 2025

References

- Fabian, J., Matos-Abiad, A., Ertler, C., Stano, P. & Žutić, I. Semiconductor spintronics. *Acta Phys. Slov.* **57**, 565 (2007).
- Žutić, I., Fabian, J. & Das Sarma, S. Spintronics: fundamentals and applications. *Rev. Mod. Phys.* **76**, 323–410 (2004).
- Maassen, T., Dejene, F. K., Guimarães, M. H. D., Józsa, C. & van Wees, B. J. Comparison between charge and spin transport in few-layer graphene. *Phys. Rev. B* **83**, 115410 (2011).
- Omar, S. & van Wees, B. J. Spin transport in high-mobility graphene on WS₂ substrate with electric-field tunable proximity spin–orbit interaction. *Phys. Rev. B* **97**, 045414 (2018).
- Omar, S. & van Wees, B. J. Graphene-WS₂ heterostructures for tunable spin injection and spin transport. *Phys. Rev. B* **95**, 081404 (2017).
- Popinciuc, M. et al. Electronic spin transport in graphene field-effect transistors. *Phys. Rev. B* **80**, 214427 (2009).
- Tombros, N., Jozsa, C., Popinciuc, M., Jonkman, H. T. & van Wees, B. J. Electronic spin transport and spin precession in single graphene layers at room temperature. *Nature* **448**, 571 (2007).
- Tombros, N. et al. Anisotropic spin relaxation in graphene. *Phys. Rev. Lett.* **101**, 046601 (2008).
- Pezo, A. et al. Manipulation of spin transport in graphene/transition metal dichalcogenide heterobilayers upon twisting. *2D Mater.* **9**, 015008 (2021).
- Volmer, F., Drögeler, M., Güntherodt, G., Stampfer, C. & Beschoten, B. Spin and charge transport in graphene-based spin transport devices with Co/MgO spin injection and spin detection electrodes. *Synth. Met.* **210**, 42 (2015).
- Garcia, J. H., Vila, M., Cummings, A. W. & Roche, S. Spin transport in graphene/transition metal dichalcogenide heterostructures. *Chem. Soc. Rev.* **47**, 3359 (2018).
- Dolui, K. et al. Proximity spin–orbit torque on a two-dimensional magnet within van der Waals heterostructure: current-driven antiferromagnet-to-ferromagnet reversible nonequilibrium phase transition in bilayer CrI₃. *Nano Lett.* **20**, 2288–2295 (2020).
- Wang, Y. & Yang, H. Spin–orbit torques based on topological materials. *Acc. Mater. Res.* **3**, 1061–1072 (2022).
- Husain, S. et al. Emergence of spin–orbit torques in 2D transition metal dichalcogenides: a status update. *Appl. Phys. Rev.* **7**, 041312 (2020).
- Manchon, A. & Yang, H. in *Spintronics Handbook, Second Edition: Spin Transport and Magnetism* 387–419 (CRC Press, 2019).
- Soumyanarayanan, A., Reyren, N., Fert, A. & Panagopoulos, C. Emergent phenomena induced by spin–orbit coupling at surfaces and interfaces. *Nature* **539**, 509–517 (2016).
- Frank, T., Högl, P., Gmitra, M., Kochan, D. & Fabian, J. Protected pseudohelical edge states in *x*₂-trivial proximitized graphene. *Phys. Rev. Lett.* **120**, 156402 (2018).
- Högl, P. et al. Quantum anomalous Hall effects in graphene from proximity-induced uniform and staggered spin–orbit and exchange coupling. *Phys. Rev. Lett.* **124**, 136403 (2020).
- Hasan, M. Z. & Kane, C. L. Colloquium: topological insulators. *Rev. Mod. Phys.* **82**, 3045–3067 (2010).
- Zhang, H. et al. Topological insulators in Bi₂Se₃, Bi₂Te₃ and Sb₂Te₃ with a single Dirac cone on the surface. *Nat. Phys.* **5**, 438–442 (2009).
- Zhang, T. et al. Experimental demonstration of topological surface states protected by time-reversal symmetry. *Phys. Rev. Lett.* **103**, 266803 (2009).
- Seiler, A. M. et al. Layer-selective spin–orbit coupling and strong correlation in bilayer graphene. Preprint at <https://arxiv.org/abs/2403.17140> (2024).
- Zhumagulov, Y., Kochan, D. & Fabian, J. Swapping exchange and spin–orbit induced correlated phases in proximitized Bernal bilayer graphene. *Phys. Rev. B* **110**, 445427 (2024).
- Zhumagulov, Y., Kochan, D. & Fabian, J. Emergent correlated phases in rhombohedral trilayer graphene induced by proximity spin–orbit and exchange coupling. *Phys. Rev. Lett.* **132**, 186401 (2024).
- Koh, J. M., Alicea, J. & Lantagne-Hurtubise, E. Correlated phases in spin–orbit-coupled rhombohedral trilayer graphene. *Phys. Rev. B* **109**, 035113 (2024).
- Gmitra, M. & Fabian, J. First-principles studies of orbital and spin–orbit properties of GaAs, GaSb, InAs, and InSb zinc-blende and wurtzite semiconductors. *Phys. Rev. B* **94**, 165202 (2016).

27. Şahin, H. et al. Monolayer honeycomb structures of group-iv elements and iii–v binary compounds: first-principles calculations. *Phys. Rev. B* **80**, 155453 (2009).
28. Xu, Y. et al. Large-gap quantum spin Hall insulators in tin films. *Phys. Rev. Lett.* **111**, 136804 (2013).
29. Feng, B. et al. Experimental realization of two-dimensional boron sheets. *Nat. Chem.* **8**, 563–568 (2016).
30. Zhang, Y., Rubio, A. & Lay, G. L. Emergent elemental two-dimensional materials beyond graphene. *J. Phys. D Appl. Phys.* **50**, 053004 (2017).
31. Kochat, V. et al. Atomically thin gallium layers from solid-melt exfoliation. *Sci. Adv.* **4**, e1701373 (2018).
32. Zhang, S. et al. Semiconducting group 15 monolayers: a broad range of band gaps and high carrier mobilities. *Angew. Chem. Int. Ed. Engl.* **55**, 1666–1669 (2016).
33. Bianco, E. et al. Stability and exfoliation of germanane: a germanium graphene analogue. *ACS Nano* **7**, 4414–4421 (2013).
34. Ji, J. et al. Two-dimensional antimonene single crystals grown by van der Waals epitaxy. *Nat. Commun.* **7**, 13352 (2016).
35. Vogt, P. et al. Silicene: compelling experimental evidence for graphene-like two-dimensional silicon. *Phys. Rev. Lett.* **108**, 155501 (2012).
36. Feng, B. et al. Evidence of silicene in honeycomb structures of silicon on Ag(111). *Nano Lett.* **12**, 3507–3511 (2012).
37. Dávila, M. E., Xian, L., Cahangirov, S., Rubio, A. & Lay, G. L. Germanene: a novel two-dimensional germanium allotrope akin to graphene and silicene. *New J. Phys.* **16**, 095002 (2014).
38. Zhu, F.-F. et al. Epitaxial growth of two-dimensional stanene. *Nat. Mater.* **14**, 1020–1025 (2015).
39. Yuhara, J., He, B., Matsunami, N., Nakatake, M. & Le Lay, G. Graphene's latest cousin: plumbene epitaxial growth on a 'nano watercube'. *Adv. Mater.* **31**, 1901017 (2019).
40. Kane, C. L. & Mele, E. J. Quantum spin Hall effect in graphene. *Phys. Rev. Lett.* **95**, 226801 (2005).
41. Liu, C.-C., Feng, W. & Yao, Y. Quantum spin Hall effect in silicene and two-dimensional germanium. *Phys. Rev. Lett.* **107**, 076802 (2011).
42. Ezawa, M. Valley-polarized metals and quantum anomalous Hall effect in silicene. *Phys. Rev. Lett.* **109**, 055502 (2012).
43. Ezawa, M. Monolayer topological insulators: silicene, germanene, and stanene. *J. Phys. Soc. Jpn* **84**, 121003 (2015).
44. Bampoulis, P. et al. Quantum spin Hall states and topological phase transition in germanene. *Phys. Rev. Lett.* **130**, 196401 (2023).
45. Gmitra, M., Konschuh, S., Ertler, C., Ambrosch-Draxl, C. & Fabian, J. Band-structure topologies of graphene: spin-orbit coupling effects from first principles. *Phys. Rev. B* **80**, 235431 (2009).
46. Reis, F. et al. Bismuthene on a SiC substrate: a candidate for a high-temperature quantum spin Hall material. *Science* **357**, 287–290 (2017).
47. Zhang, W. et al. Epitaxial synthesis of blue phosphorene. *Small* **14**, 1804066 (2018).
48. Aktürk, O. U., Özçelik, V. O. & Ciraci, S. Single-layer crystalline phases of antimony: antimonenes. *Phys. Rev. B* **91**, 235446 (2015).
49. Liu, H. et al. Phosphorene: an unexplored 2D semiconductor with a high hole mobility. *ACS Nano* **8**, 4033–4041 (2014).
50. Asahina, H., Shindo, K. & Morita, A. Electronic structure of black phosphorus in self-consistent pseudopotential approach. *J. Phys. Soc. Jpn* **51**, 1193–1199 (1982).
51. Li, L. et al. Black phosphorus field-effect transistors. *Nat. Nanotechnol.* **9**, 372–377 (2014).
52. Wang, X. et al. Highly anisotropic and robust excitons in monolayer black phosphorus. *Nat. Nanotechnol.* **10**, 517–521 (2015).
53. Aysar, A. et al. Gate-tunable black phosphorus spin valve with nanosecond spin lifetimes. *Nat. Phys.* **13**, 888 (2017).
54. Shiff, L. I. *Quantum Mechanics* (McGraw-Hill Education, 1968).
55. Landau, L. D. & Lifshitz, E. M. *Quantum Mechanics Non-Relativistic Theory* (Pergamon Press, 1977).
56. Kurpas, M., Junior, P. E. F., Gmitra, M. & Fabian, J. Spin-orbit coupling in elemental two-dimensional materials. *Phys. Rev. B* **100**, 125422 (2019).
57. Elliott, R. J. Theory of the effect of spin-orbit coupling on magnetic resonance in some semiconductors. *Phys. Rev.* **96**, 266–279 (1954).
58. MacDonald, A. H. & Vosko, S. H. A relativistic density functional formalism. *J. Phys. C Solid State Phys.* **12**, 2977 (1979).
59. Rajagopal, A. K. & Callaway, J. Inhomogeneous electron gas. *Phys. Rev. B* **7**, 1912–1919 (1973).
60. Giannozzi, P. et al. Quantum espresso toward the exascale. *J. Chem. Phys.* **152**, 154105 (2020).
61. Kresse, G. & Furthmüller, J. Efficient iterative schemes for ab initio total-energy calculations using a plane-wave basis set. *Phys. Rev. B* **54**, 11169–11186 (1996).
62. Kleinman, L. Relativistic norm-conserving pseudopotential. *Phys. Rev. B* **21**, 2630–2631 (1980).
63. Bachelet, G. B. & Schlüter, M. Relativistic norm-conserving pseudopotentials. *Phys. Rev. B* **25**, 2103–2108 (1982).
64. Corso, A. D. & Conte, A. M. Spin-orbit coupling with ultrasoft pseudopotentials: application to Au and Pt. *Phys. Rev. B* **71**, 115106 (2005).
65. Blaha, P. et al. WIEN2k: an APW+lo program for calculating the properties of solids. *J. Chem. Phys.* **152**, 074101 (2020).
66. Gulans, A. et al. Exciting: a full-potential all-electron package implementing density-functional theory and many-body perturbation theory. *J. Condens. Matter Phys.* **26**, 363202 (2014).
67. The ELK project. <http://elk.sourceforge.net/>.
68. The FLEUR project. <https://www.flapw.de/>.
69. Singh, D. J. & Nordström, L. *Planewaves, Pseudopotentials, and the LAPW Method* (Springer, 2005).
70. Vona, C., Lubeck, S., Kleine, H., Gulans, A. & Draxl, C. Accurate and efficient treatment of spin-orbit coupling via second variation employing local orbitals. *Phys. Rev. B* **108**, 235161 (2023).
71. Zimmermann, B. et al. Anisotropy of spin relaxation in metals. *Phys. Rev. Lett.* **109**, 236603 (2012).
72. Fabian, J. & Das Sarma, S. Spin relaxation of conduction electrons in polyvalent metals: theory and a realistic calculation. *Phys. Rev. Lett.* **81**, 5624–5627 (1998).
73. Mokrousov, Y. et al. Anisotropy of spin relaxation and transverse transport in metals. *J. Condens. Matter Phys.* **25**, 163201 (2013).
74. Jureczko, P., Haniš, J., Faria Junior, P. E., Gmitra, M. & Kurpas, M. Probing type-II Ising pairing using the spin-mixing parameter. *Phys. Rev. B* **109**, 165428 (2024).
75. Wang, C. et al. Type-II Ising superconductivity in two-dimensional materials with spin-orbit coupling. *Phys. Rev. Lett.* **123**, 126402 (2019).
76. Falson, J. et al. Type-II Ising pairing in few-layer stanene. *Science* **367**, 1454–1457 (2020).
77. Yafet, Y. g factors and spin-lattice relaxation of conduction electrons. In *Solid State Physics* Vol. 14, 1–98 (Academic Press, 1963).
78. Eschrig, H. *Optimized LCAO Method and the Electronic Structure of Extended Systems* (Akademie-Verlag, 1988).
79. Manzeli, S., Ovchinnikov, D., Pasquier, D., Yazyev, O. V. & Kis, A. 2d transition metal dichalcogenides. *Nat. Rev. Mater.* **2**, 17033 (2017).
80. Chernikov, A. et al. Exciton binding energy and nonhydrogenic Rydberg series in monolayer WS₂. *Phys. Rev. Lett.* **113**, 076802 (2014).
81. Xiao, D., Liu, G.-B., Feng, W., Xu, X. & Yao, W. Coupled spin and valley physics in monolayers of MoS₂ and other group-VI dichalcogenides. *Phys. Rev. Lett.* **108**, 196802 (2012).
82. Tao, Y., Schneeloch, J. A., Aczel, A. A. & Louca, D. T_d to 1T' structural phase transition in the WTe₂ Weyl semimetal. *Phys. Rev. B* **102**, 060103 (2020).
83. Kormányos, A. et al. k.p theory for two-dimensional transition metal dichalcogenide semiconductors. *2D Mater.* **2**, 022001 (2015).
84. Grüner, G. The dynamics of charge-density waves. *Rev. Mod. Phys.* **60**, 1129–1181 (1988).
85. Chen, P. et al. Charge density wave transition in single-layer titanium diselenide. *Nat. Commun.* **6**, 8943 (2015).
86. Sipos, B. et al. From Mott state to superconductivity in 1T-TaS₂. *Nat. Mater.* **7**, 960–965 (2008).
87. Moncton, D. E., Axe, J. D. & DiSalvo, F. J. Neutron scattering study of the charge-density wave transitions in 2H-TaSe₂ and 2H-NbSe₂. *Phys. Rev. B* **16**, 801–819 (1977).
88. Ishioka, J. et al. Chiral charge-density waves. *Phys. Rev. Lett.* **105**, 176401 (2010).
89. Castellan, J.-P. et al. Chiral phase transition in charge ordered 1T-TiSe₂. *Phys. Rev. Lett.* **110**, 196404 (2013).
90. Peng, Y. et al. Observation of orbital order in the van der Waals material 1T-TiSe₂. *Phys. Rev. Res.* **4**, 033053 (2022).
91. Xu, S.-Y. et al. Spontaneous gyrotropic electronic order in a transition-metal dichalcogenide. *Nature* **578**, 545–549 (2020).
92. Gao, J. J. et al. Chiral charge density waves induced by Ti-doping in 1T-TaS₂. *Appl. Phys. Lett.* **118**, 213105 (2021).
93. Zhao, Y. et al. Spectroscopic visualization and phase manipulation of chiral charge density waves in 1T-TaS₂. *Nat. Commun.* **14**, 2223 (2023).
94. Song, X. et al. Atomic-scale visualization of chiral charge density wave superlattices and their reversible switching. *Nat. Commun.* **13**, 1843 (2022).
95. Xi, X. et al. Strongly enhanced charge-density-wave order in monolayer NbSe₂. *Nat. Nanotechnol.* **10**, 765–769 (2015).
96. Ugeda, M. M. et al. Characterization of collective ground states in single-layer NbSe₂. *Nat. Phys.* **12**, 92–97 (2016).
97. Dreher, P. et al. Proximity effects on the charge density wave order and superconductivity in single-layer NbSe₂. *ACS Nano* **15**, 19430–19438 (2021).
98. Liu, X., Chong, Y. X., Sharma, R. & Davis, J. C. S. Discovery of a cooper-pair density wave state in a transition-metal dichalcogenide. *Science* **372**, 1447–1452 (2021).
99. von Rohr, F. O. et al. Unconventional scaling of the superfluid density with the critical temperature in transition metal dichalcogenides. *Sci. Adv.* **5**, eaav8465 (2019).
100. Lu, J. M. et al. Evidence for two-dimensional Ising superconductivity in gated MoS₂. *Science* **350**, 1353–1357 (2015).
101. Xi, X. et al. Ising pairing in superconducting NbSe₂ atomic layers. *Nat. Phys.* **12**, 139–143 (2016).
102. Chen, P. et al. Large quantum-spin-Hall gap in single-layer 1T' WSe₂. *Nat. Commun.* **9**, 2003 (2018).
103. Jiang, J. et al. Signature of type-II Weyl semimetal phase in MoTe₂. *Nat. Commun.* **8**, 13973 (2017).
104. Li, P. et al. Evidence for topological type-II Weyl semimetal WTe₂. *Nat. Commun.* **8**, 2150 (2017).
105. Li, Z., Song, Y. & Tang, S. Quantum spin Hall state in monolayer 1T'-TMDCs. *J. Condens. Matter Phys.* **32**, 333001 (2020).

106. Tang, S. et al. Quantum spin Hall state in monolayer 1T'-WTe₂. *Nat. Phys.* **13**, 683–687 (2017).
107. Mostofi, A. A. et al. An updated version of wannier90: a tool for obtaining maximally-localised Wannier functions. *Comput. Phys. Commun.* **185**, 2309–2310 (2014).
108. Wu, Q., Zhang, S., Song, H.-F., Troyer, M. & Soluyanov, A. A. Wanniertools: an open-source software package for novel topological materials. *Comput. Phys. Commun.* **224**, 405–416 (2018).
109. Cepellotti, A., Coulter, J., Johansson, A., Fedorova, N. S. & Kozinsky, B. Phoebe: a high-performance framework for solving phonon and electron Boltzmann transport equations. *J. Phys. Mater.* **5**, 035003 (2022).
110. Kaloni, T. P., Kou, L., Frauenheim, T. & Schwingenschlögl, U. Quantum spin Hall states in graphene interacting with WS₂ or WSe₂. *Appl. Phys. Lett.* **105**, 233112 (2014).
111. Gmitra, M. & Fabian, J. Graphene on transition-metal dichalcogenides: a platform for proximity spin–orbit physics and optospintronics. *Phys. Rev. B* **92**, 155403 (2015).
112. Island, J. O. et al. Spin–orbit-driven band inversion in bilayer graphene by the van der Waals proximity effect. *Nature* **571**, 85 (2019).
113. Gmitra, M., Kochan, D., Högl, P. & Fabian, J. Trivial and inverted Dirac bands and the emergence of quantum spin Hall states in graphene on transition-metal dichalcogenides. *Phys. Rev. B* **93**, 155104 (2016).
114. Khatibi, Z. & Power, S. R. Proximity spin–orbit coupling in graphene on alloyed transition metal dichalcogenides. *Phys. Rev. B* **106**, 125417 (2022).
115. Zollner, K., Faria Junior, P. E. & Fabian, J. Proximity exchange effects in MoSe₂ and WSe₂ heterostructures with CrI₃: twist angle, layer, and gate dependence. *Phys. Rev. B* **100**, 085128 (2019).
116. Konschuh, S., Gmitra, M., Kochan, D. & Fabian, J. Theory of spin–orbit coupling in bilayer graphene. *Phys. Rev. B* **85**, 115423 (2012).
117. Zollner, K., Gmitra, M. & Fabian, J. Swapping exchange and spin–orbit coupling in 2d van der Waals heterostructures. *Phys. Rev. Lett.* **125**, 196402 (2020).
118. Zollner, K. & Fabian, J. Bilayer graphene encapsulated within monolayers of WS₂ or Cr₂Ge₂Te₆: tunable proximity spin–orbit or exchange coupling. *Phys. Rev. B* **104**, 075126 (2021).
119. Zollner, K., Junior, P. E. F. & Fabian, J. Strain-tunable orbital, spin–orbit, and optical properties of monolayer transition-metal dichalcogenides. *Phys. Rev. B* **100**, 195126 (2019).
120. Lanzillo, N. A., Simbeck, A. J. & Nayak, S. K. Strain engineering the work function in monolayer metal dichalcogenides. *J. Condens. Matter Phys.* **27**, 175501 (2015).
121. Grassano, D. et al. Work function, deformation potential, and collapse of Landau levels in strained graphene and silicene. *Phys. Rev. B* **101**, 245115 (2020).
122. Choi, S.-M., Jhi, S.-H. & Son, Y.-W. Effects of strain on electronic properties of graphene. *Phys. Rev. B* **81**, 081407 (2010).
123. Pereira, V. M., Castro Neto, A. H. & Peres, N. M. R. Tight-binding approach to uniaxial strain in graphene. *Phys. Rev. B* **80**, 045401 (2009).
124. Wunsch, B., Guinea, F. & Sols, F. Dirac-point engineering and topological phase transitions in honeycomb optical lattices. *New J. Phys.* **10**, 103027 (2008).
125. Naimer, T., Zollner, K., Gmitra, M. & Fabian, J. Twist-angle dependent proximity induced spin–orbit coupling in graphene/transition metal dichalcogenide heterostructures. *Phys. Rev. B* **104**, 195156 (2021).
126. Zollner, K., João, S. M., Nikolić, B. K. & Fabian, J. Twist- and gate-tunable proximity spin–orbit coupling, spin relaxation anisotropy, and charge-to-spin conversion in heterostructures of graphene and transition metal dichalcogenides. *Phys. Rev. B* **108**, 235166 (2023).
127. David, A., Rakya, P., Kormányos, A. & Burkard, G. Induced spin–orbit coupling in twisted graphene–transition metal dichalcogenide heterobilayers: twistronics meets spintronics. *Phys. Rev. B* **100**, 085412 (2019).
128. Li, Y. & Koshino, M. Twist-angle dependence of the proximity spin–orbit coupling in graphene on transition-metal dichalcogenides. *Phys. Rev. B* **99**, 075438 (2019).
129. Lee, S. et al. Charge-to-spin conversion in twisted graphene/WSe₂ heterostructures. *Phys. Rev. B* **106**, 165420 (2022).
130. Yang, H. et al. Twist-angle tunable spin texture in WSe₂/graphene van der Waals heterostructures. *Nat. Mater.* **23**, 1502–1508 (2024).
131. Veneri, A., Perkins, D. T. S., Péterfalvi, C. G. & Ferreira, A. Twist angle controlled collinear Edelstein effect in van der Waals heterostructures. *Phys. Rev. B* **106**, L081406 (2022).
132. Frank, T., Faria Junior, P. E., Zollner, K. & Fabian, J. Emergence of radial Rashba spin–orbit fields in twisted van der Waals heterostructures. *Phys. Rev. B* **109**, L241403 (2024).
133. Hoque, A. M. et al. All-electrical creation and control of spin-galvanic signal in graphene and molybdenum ditelluride heterostructures at room temperature. *Commun. Phys.* **4**, 124 (2021).
134. Zollner, K., Gmitra, M., Frank, T. & Fabian, J. Theory of proximity-induced exchange coupling in graphene on hBN/(Co, Ni). *Phys. Rev. B* **94**, 155441 (2016).
135. Fülöp, B. et al. Boosting proximity spin–orbit coupling in graphene/WSe₂ heterostructures via hydrostatic pressure. *NPJ 2D Mater. Appl.* **5**, 82 (2021).
136. Fülöp, B. et al. New method of transport measurements on van der Waals heterostructures under pressure. *J. Appl. Phys.* **130**, 064303 (2021).
137. Zollner, K. & Fabian, J. Proximity effects in graphene on monolayers of transition-metal phosphorus trichalcogenides mPX₃ (m: Mn, Fe, Ni, Co, and X: S, Se). *Phys. Rev. B* **106**, 035137 (2022).
138. Miliivojević, M., Gmitra, M., Karpas, M., Štić, I. & Fabian, J. Giant asymmetric proximity-induced spin–orbit coupling in twisted graphene/SnTe heterostructure. *2D Mater.* **11**, 035036 (2024).
139. Song, K. et al. Spin proximity effects in graphene/topological insulator heterostructures. *Nano Lett.* **18**, 2033 (2018).
140. Zihlmann, S. et al. Large spin relaxation anisotropy and valley-Zeeman spin–orbit coupling in WSe₂/graphene/h-BN heterostructures. *Phys. Rev. B* **97**, 075434 (2018).
141. Stawińska, J. & Cerdá, J. I. Complex spin texture of Dirac cones induced via spin–orbit proximity effect in graphene on metals. *Phys. Rev. B* **98**, 075436 (2018).
142. Khokhriakov, D. et al. Tailoring emergent spin phenomena in Dirac material heterostructures. *Sci. Adv.* **4**, eaat9349 (2018).
143. Ghiasi, T. S., Ingla-Aynés, J., Kaverzin, A. A. & Van Wees, B. J. Large proximity-induced spin lifetime anisotropy in transition-metal dichalcogenide/graphene heterostructures. *Nano Lett.* **17**, 7528 (2017).
144. Benítez, L. A. et al. Strongly anisotropic spin relaxation in graphene-transition metal dichalcogenide heterostructures at room temperature. *Nat. Phys.* **14**, 303 (2018).
145. Herling, F. et al. Gate tunability of highly efficient spin-to-charge conversion by spin Hall effect in graphene proximitized with WSe₂. *APL Mater.* **8**, 071103 (2020).
146. Ontoso, N. et al. Unconventional charge-to-spin conversion in graphene/MoTe₂ van der Waals heterostructures. *Phys. Rev. Appl.* **19**, 014053 (2023).
147. Safeer, C. et al. Large multidirectional spin-to-charge conversion in low-symmetry semimetal MoTe₂ at room temperature. *Nano Lett.* **19**, 8758–8766 (2019).
148. Haugen, H., Huertas-Hernando, D. & Brataas, A. Spin transport in proximity-induced ferromagnetic graphene. *Phys. Rev. B* **77**, 115406 (2008).
149. Wang, Z., Tang, C., Sachs, R., Barlas, Y. & Shi, J. Proximity-induced ferromagnetism in graphene revealed by the anomalous Hall effect. *Phys. Rev. Lett.* **114**, 016603 (2015).
150. Yang, H. X. et al. Proximity effects induced in graphene by magnetic insulators: first-principles calculations on spin filtering and exchange-splitting gaps. *Phys. Rev. Lett.* **110**, 046603 (2013).
151. Karpiak, B. et al. Magnetic proximity in a van der Waals heterostructure of magnetic insulator and graphene. *2D Mater.* **7**, 015026 (2019).
152. Ghiasi, T. S. et al. Electrical and thermal generation of spin currents by magnetic bilayer graphene. *Nat. Nanotechnol.* **16**, 788–794 (2021).
153. Kaverzin, A. A., Ghiasi, T. S., Dismukes, A. H., Roy, X. & van Wees, B. J. Spin injection by spin–charge coupling in proximity induced magnetic graphene. *2D Mater.* **9**, 045003 (2022).
154. Yang, B. et al. Electrostatically controlled spin polarization in graphene-CrSBr magnetic proximity heterostructures. *Nat. Commun.* **15**, 4459 (2024).
155. Zollner, K. & Fabian, J. Engineering proximity exchange by twisting: reversal of ferromagnetic and emergence of antiferromagnetic Dirac bands in graphene/Cr₂Ge₂Te₆. *Phys. Rev. Lett.* **128**, 106401 (2022).
156. Zollner, K. et al. Scattering-induced and highly tunable by gate damping-like spin–orbit torque in graphene doubly proximitized by two-dimensional magnet Cr₂Ge₂Te₆ and monolayer WS₂. *Phys. Rev. Res.* **2**, 043057 (2020).
157. Yakovkin, I. Spin–orbit band gaps and destruction of Dirac cones. *Surf. Sci.* **662**, 1–5 (2017).
158. Liang, L. et al. Electronic bandgap and edge reconstruction in phosphorene materials. *Nano Lett.* **14**, 6400–6406 (2014).
159. Scharf, B., Xu, G., Matos-Abiad, A. & Žutić, I. Magnetic proximity effects in transition-metal dichalcogenides: converting excitons. *Phys. Rev. Lett.* **119**, 127403 (2017).
160. Yokoi, M. et al. Negative resistance state in superconducting NbSe₂ induced by surface acoustic waves. *Sci. Adv.* **6**, eaab1377 (2020).
161. Nakata, Y. et al. Robust charge-density wave strengthened by electron correlations in monolayer 1T-TaSe₂ and 1T-NbSe₂. *Nat. Commun.* **12**, 5873 (2021).
162. Zhang, X. et al. Room-temperature intrinsic ferromagnetism in epitaxial CrTe₂ ultrathin films. *Nat. Commun.* **12**, 2492 (2021).
163. Guan, M.-X., Wang, E., You, P.-W., Sun, J.-T. & Meng, S. Manipulating Weyl quasiparticles by orbital-selective photoexcitation in WTe₂. *Nat. Commun.* **12**, 1885 (2021).
164. Kochan, D., Irmer, S. & Fabian, J. Model spin–orbit coupling Hamiltonians for graphene systems. *Phys. Rev. B* **95**, 165415 (2017).
165. McClure, J. W. & Yafet, Y. Theory of the g-factor of the current carriers in graphite single crystals. In *Proc. Fifth Conference on Carbon* 22–28 (Pergamon Press, 1962).
166. Bychkov, Y. A. & Rashba, E. I. Oscillatory effects and the magnetic susceptibility of carriers in inversion layers. *J. Phys. C Solid State Phys.* **17**, 6039 (1984).
167. Péterfalvi, C. G., David, A., Rakya, P., Burkard, G. & Kormányos, A. Quantum interference tuning of spin–orbit coupling in twisted van der Waals trilayers. *Phys. Rev. Res.* **4**, L022049 (2022).
168. Szałowski, K., Miliivojević, M., Kochan, D. & Gmitra, M. Spin–orbit and exchange proximity couplings in graphene/1T-TaS₂ heterostructure triggered by a charge density wave. *2D Mater.* **10**, 025013 (2023).
169. Chi, Z. et al. Control of charge–spin interconversion in van der Waals heterostructures with chiral charge density waves. *Adv. Mater.* **36**, 2310768 (2024).
170. Frank, T., Gmitra, M. & Fabian, J. Theory of electronic and spin–orbit proximity effects in graphene on Cu(111). *Phys. Rev. B* **93**, 155142 (2016).
171. Virtanen, P. et al. SciPy 1.0: fundamental algorithms for scientific computing in Python. *Nat. Methods* **17**, 261–272 (2020).
172. Newville, M., Stensitzki, T., Allen, D. B. & Ingargiola, A. LMFIT: non-linear least-square minimization and curve-fitting for Python. *Zenodo* <https://doi.org/10.5281/zenodo.11813> (2014).

173. Eaton, J. W., Bateman, D., Hauberg, S. & Wehbring, R. *GNU Octave Version 3.8.1 Manual: A High-Level Interactive Language for Numerical Computations* (CreateSpace Independent Publishing Platform, 2014).
174. Lazic, P. CellMatch: combining two unit cells into a common supercell with minimal strain. *Comput. Phys. Commun.* **197**, 324–334 (2015).
175. Koda, D. S., Bechstedt, F., Marques, M. & Teles, L. K. Coincidence lattices of 2d crystals: heterostructure predictions and applications. *J. Phys. Chem. C* **120**, 10895–10908 (2016).
176. Bahn, S. R. & Jacobsen, K. W. An object-oriented scripting interface to a legacy electronic structure code. *Comput. Sci. Eng.* **4**, 56–66 (2002).

Acknowledgements

K.Z. and J.F. acknowledge funding through the Deutsche Forschungsgemeinschaft (DFG, German Research Foundation), SFB 1277 (Project No. 314695032), DFG SPP 2244 (Project No. 443416183), Horizon Europe Project 101135853 (2DSPIN-TECH) and FLAGERA project 2DSOTECH. M.G. acknowledges support from the Slovak Research and Development Agency under Contract No. APVV SK-CZ-RD-21-0114, Slovak Academy of Sciences project IMPULZ IM-2021-42, and Ministry of Education, Research, Development and Youth the Slovak Republic provided under Grant No. VEGA 1/0104/25. M.K. acknowledges financial support from the National Center for Research and Development under the V4-Japan project BGapEng V4-JAPAN/2/46/BGapEng/2022.

Author contributions

The authors contributed equally to all aspects of the article.

Competing interests

The authors declare no competing interests.

Additional information

Peer review information *Nature Reviews Physics* thanks the anonymous reviewers for their contribution to the peer review of this work.

Publisher's note Springer Nature remains neutral with regard to jurisdictional claims in published maps and institutional affiliations.

Springer Nature or its licensor (e.g. a society or other partner) holds exclusive rights to this article under a publishing agreement with the author(s) or other rightsholder(s); author self-archiving of the accepted manuscript version of this article is solely governed by the terms of such publishing agreement and applicable law.

© Springer Nature Limited 2025